

國立交通大學
光電工程研究所

碩士論文

鈦酸鋇隨著顆粒大小變化之晶格動力學特性
研究

Grain size effect on the lattice dynamics of barium
titanate nanoparticles



研究生：王玫丹

指導教授：謝文峰 教授

中華民國九十六年六月

鈦酸鋇隨著顆粒大小變化之晶格動力學特
性研究

Grain size effect on the lattice dynamics of
barium titanate nanoparticles

研究生：王玫丹

Student: Mei-Tan Wang

指導教授：謝文峰 教授

Advisor: Dr. Wen-Feng Hsieh



A Thesis
Submitted to Institute of Electro-Optical Engineering
College of Electrical Engineering and Computer Science
National Chiao Tung University
In partial Fulfillment of the Requirements
For the Degree of
Master
in
Electro-Optical Engineering
June 2007
Hsin-chu, Taiwan, Republic of China

中華民國九十六年六月

致謝

碩士班兩年，首先感謝謝文峰教授對我學習研究上的指導，再來就是感謝很罩我的黃董，感謝他對我碩班兩年實驗或理論上的幫助與建議，另外感謝其他實驗室學長姐的幫助。接著就是跟我一起相處兩年的碩二的同學們，不管在學業上或玩樂上，讓我這兩年的生活都很愉快，希望大家畢業後都能順利做想做的事。



2006年6月于交大

鈦酸鋇隨著顆粒大小變化之晶格動力學特性研究

研究生：王玫丹

指導教授：謝文峰 教授

國立交通大學光電工程研究所

摘要

我們利用掃描式電子顯微鏡、高解析度 X 光繞射儀及拉曼光譜來研究鈦酸鋇奈米顆粒小於 60nm 的物理特性；樣品的製程採用甘油反應法。藉由使用 GSAS 的軟體模擬 XRD 的數據(使用 Rietveld refinement 的方法)，我們可以發現當顆粒大小減少時，正方晶相的組成變少且單位晶胞的體積變大的情形。此外，我們考慮三各 $A_1(\text{TO})$ 模態的非簡諧的耦合情況，得出原來在 180 cm^{-1} 的光譜圖附近的 dip 會變成 peak，是由於 $A_1(\text{TO}_1)$ 、 $A_2(\text{TO})$ 兩各模態的耦合變弱造成。根據之前 Kuo's report [PRB. 64, 224103-1 (2001)]，對 $\text{Ba}_{1-x}\text{Sr}_x\text{TiO}_3$ 系統而言，改變單位晶胞體積的大小是造成 LO-TO splitting 的主要因素(忽略等效電荷的改變)。在我們的研究中，我們藉由減少顆粒大小(單位晶胞體積變大)直接觀察到 LO-TO splitting 減小的效應。

Grain size effect on the lattice dynamics of barium titanate nanoparticles

Student: Mei-Tan Wang

Advisor: Prof. Wen-Feng Hsieh

Institute of Electro-optical Engineering

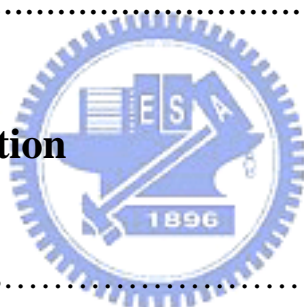
National Chaio Tung University

Abstract

We report SEM, XRD and Raman studies of BaTiO₃ fine nanoparticles with diameter less than 60 nm synthesized by glycothermal reaction. Through the GSAS Rietveld refinement of XRD data, we found decreasing the size of BaTiO₃ nanoparticles causes less tetragonality and expansion of the unit-cell volume. By taking the anharmonic coupling between the three A₁(TO) modes into account, we attributed the disappear of spectral interference dip at ~180 cm⁻¹ assigned to A₁(TO₁) to the weaker coupling between A₁(TO) and A₂(TO) modes. According to Kuo's report [PRB. 64, 224103-1 (2001)], the change of unit-cell volume is the dominant mechanism of change of the LO–TO splitting in Ba_{1-x}Sr_xTiO₃ system with negligible change of effective charge due to the substitution. In this study, we directly observed the decreasing LO-TO splitting with the decline of tetragonality by decreasing the size of BaTiO₃ nanoparticles which causes expansion of the unit-cell volume.

Table of Contents

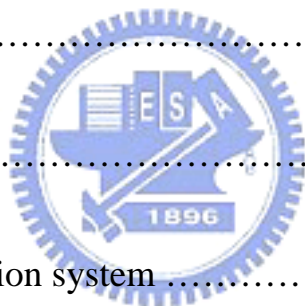
Abstract (in English)	i
Abstract (in Chinese)	ii
Acknowledgments	iii
List of Figures	vii
List of Tables	x
Chapter 1 Introduction	
1.1 Ferroelectric materials.....	1
1.2 Perovskites	1
1.3 Motivation.....	3
1.4 Organization of the thesis.....	5
Chapter 2 Theoretical Background	
2.1 X-ray diffraction.....	6
2.2 Rietveld method	9



2.2-1 Core Mathematics and Procedure	10
2.2-2 Criteria of Fit	11
2.2-3 The profile fuction	12
2.3 Raman scattering.....	13
2.4 Born effective charges and LO-TO splitting.....	14

Chapter 3 Experimental Details

3.1 Sample preparation.....	18
3.2 Characterization.....	21
3.2.1 X-ray diffraction system	21
3.2.2 Refinement system.....	21
3.2.3 Raman detection system.....	21
3.3 Refinement procedure.....	23



Chapter 4 Results and Discussion

4. 1 Results of the SEM patterns	27
4.2 Analysis of Rietveld method	28

4.3 Analysis of the Raman spectra.....33

Chapter 5 Conclusion

5.1 Conclusion42

5.2 Future Works.....43

References.....44



List of Tables

Table 4.1 The structural parameter of BaTiO ₃	28
Table 4.2 Refined structure parameters and reliability factors for BaTiO ₃ nanoparticles at RT.....	31



Chapter 1 Introduction

1.1 Ferroelectric materials

Ferroelectricity is a phenomenon which has spontaneous polarization when cooling below the Curie point, ferroelectric domains, ferroelectric hysteresis loop and so on. Ferroelectric ceramics were produced in the early 1940s with the discovery of the phenomenon of ferroelectricity with the high dielectric constant in barium titanate (BaTiO_3). Complex oxide perovskites possessing ferroelectric property have versatile applications, for example, ceramic capacitors in bulk forms and in the forms of thin films for ferroelectric random access memory, infrared pyroelectric sensors, transistors, microwave electronics, and electro-optic modulators, etc. Owing to its excellent ferroelectric properties, barium titanate (BaTiO_3) is one of the most generally investigated ferroelectric materials among the complex oxide perovskites.

[1]

1.2 Perovskites

The perovskite compounds are an extremely important group of ferroelectric materials. Perovskite-type structured materials exhibit useful properties and have a variety of crystal structure. The general formula of perovskites is ABX_3 (see Fig. 1.1), which is composed of three distinct chemical elements in the ratios of 1:1:3. The “A” and “B” are metallic elements and the “X” is a non-metallic element. The “A” and “B” represent +2 and +4 ions, respectively, while the “X” is the O^{2-} ion. The “A” metallic ion is usually larger than “B” metallic one in the perovskite structure. The ABO_3 structure in a general sense can be thought of as a

face-centered cubic (FCC) lattice with “A” ions at the corners, the Oxygen ions on the faces and the “B” ion at the center of the lattice (see Fig. 1.2).

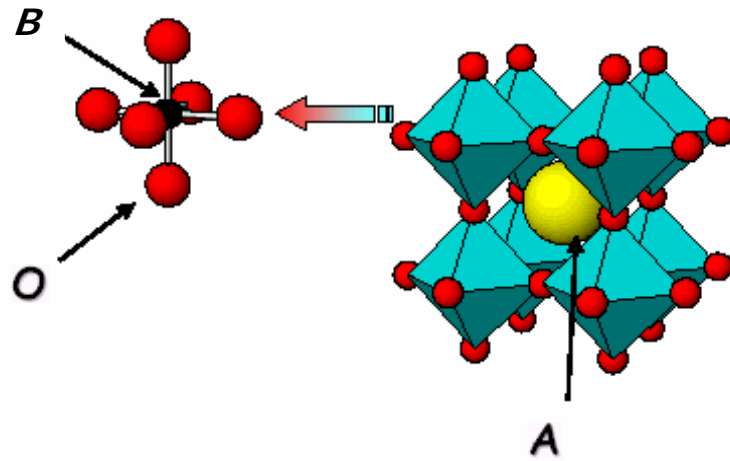


Figure 1.1 Perovskite structure

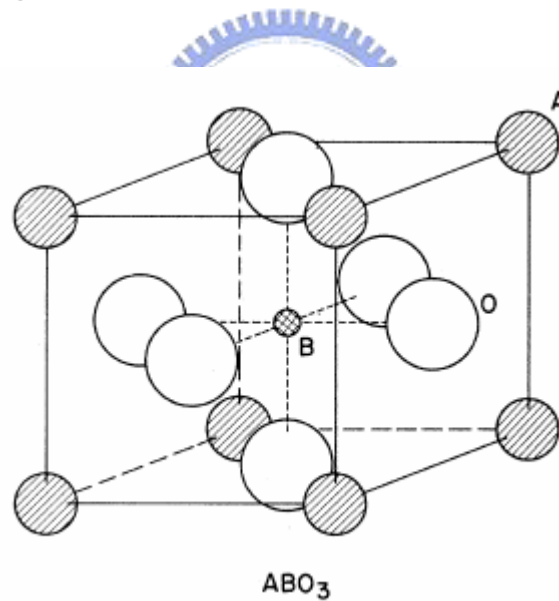


Figure 1.2 ABO₃ structure

As a stronger electric field is applied to the ABO₃-type perovskite, the “B” cation will displace from the original octahedron. Shifting of this “B” cation due to the applied electric field causes the change of structure, in turn induces electric dipole.

The atomic structure of perovskite is very sensitive to the alteration in the factor of temperature. As the temperature changes, the crystallographic dimensions change

due to distortion of the octahedral. The crystal structures of ABO_3 include cubic, tetragonal, orthorhombic, and rhombohedral [1,3](see Fig. 1.3).

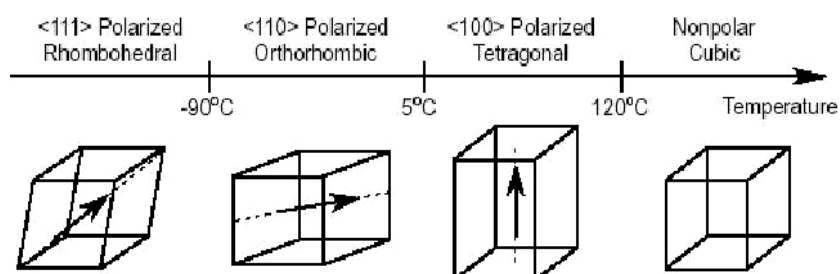


Figure 1.3 Phases of $BaTiO_3$

All of the ferroelectric materials have a transition temperature called the Curie point (T_c). When the crystal temperature goes above the Curie point, $T > T_c$, the crystal doesn't exhibit ferroelectricity, while for $T < T_c$ the crystal exhibits ferroelectricity. Decreasing the temperature around the Curie point, a ferroelectric crystal undergoes a phase transition from a non-ferroelectric phase to a ferroelectric phase. As a result, the distorted octahedral are coupled together, and a very large spontaneous polarization can be achieved. This large spontaneous polarization will lead to a large dielectric constant highly sensitive to the distorted structure.

1.3 Motivation

The continuous advance in miniaturization of ferroelectric devices, $BaTiO_3$ fine particles as a ferroelectric material have been applied in advanced electric devices [2] such as multilayer ceramic capacitor, and their physical properties have been dramatically influenced by various effects, such as temperature [3-5], pressure [4,6], substitution [7], and size [8-12]. Among them, due to the close relationship between

ferroelectric properties and crystal structure, the size dependence of structure is presently the major research topics.

The ferroelectric transition occurs as a result of balance between long-range Coulomb interaction and short-range forces [14]. Particularly, the Coulomb interaction makes the ferroelectric sensitive in response to details of domain structure, defect, and boundary conditions. Another direct effect of such interaction is the splitting of longitudinal optical (LO) and transverse optical (TO) phonons. The Born dynamical effective charges play a central role in the study of these Coulomb effects. However, early calculations did not directly address the role of Coulomb interactions until giant LO-TO splitting had performed in ABO_3 cubic perovskite compounds using local density approximation (LDA) by Zhong et al [14]. Previously studying on $Ba_xSr_{1-x}TiO_3$ (BST) system [7], had reported the repulsion of giant LO-TO splitting when tetragonal to cubic phase transition occurs, and it was explained as a result of decreasing cell dimension and strengthening the electron-phonon coupling, which was the first experimental evidence for the lattice dynamics related to the Coulomb interaction.

In the previous study of $Ba_xSr_{1-x}TiO_3$ (BST) system [7], the repulsion of giant LO-TO splitting with increasing “Sr” substitution, which causes crystal structure to change from tetragonal phase toward cubic phase, is due to decrease in the dimensions of the unit cell. In contract to that in BST system, we report this thesis, the attractive LO-TO splitting behavior and crystal structure change from the tetragonal phase toward the cubic for reducing diameter of $BaTiO_3$ nanocrystals from 140 nm to 30 nm.

1.4 Organization of the thesis

There are five chapters in this thesis. In Chapter 2, we first describe the related theoretic background such as lattice structure and lattice dynamics. Chapter 3 describes the experimental details, including sample preparation by the glycothermal methods and equipment setups. We will give the results and discussion about the size effect on the BaTiO₃ system including phase transition and LO-TO splitting. The dominant mechanism on LO-TO splitting is in Chapter 4. In the final chapter, we conclude the investigations on the BaTiO₃ nanoparticles and proposed several topics worthy of further studying.



Chapter 2 Theoretical Background

2.1 X-ray diffraction

For the particular condition described by Fig. 2-1, the only diffracted beam form is that shown, namely one making an angle of reflection θ equal to the angle of incident θ . We will show this, first, for one plane of atoms and, second, for all the atoms making up the crystal. Consider rays **1** and **1a** of the incident beam, they strike atoms *K* and *P* on the first plane of the crystal and are scattered in all directions. While in the directions **1'** and **1a'** of the scattered beams are completely in phase capable of reinforcing each other; because the path difference between the wave fronts **XX'** and **YY'** is equal

$$QK - PR = PK \cos \theta - PK \sin \theta = 0 . \quad (2.1)$$

Similarly, the scattered rays from all the atoms on the first plane to the directions parallel to **1'** are in phase contribute to the diffracted beam. This will be true for all of the planes, and it remains to find the condition of rays scattered by atoms on the different planes. Consider parallel lattice planes spaced d' apart. Rays **1** and **2**, for example, are scattered by atoms *K* and *L*, and the path difference of the rays **1KI'** and **2L2'**,

$$ML + LN = d' \sin \theta + d' \sin \theta \quad (2.2)$$

is equal to the path difference of the overlapping rays scattered by *S* and *P* in the same direction shown in Fig. 2.1, since in this direction there is no path difference between rays scattered by *S* and *L* or *P* and *K*. The scattered rays **1'** and **2'** will be completely in phase if the path difference is equal to an integer number n of wavelengths λ , i.e.,

$$n \lambda = 2d' \sin \theta . \quad (2.3)$$

This relation was first formulated by Bragg and is known as the Bragg's law. Assuming $n = 1$, we can consider a reflection of any order as a first-order reflection from planes, real or fictitious, spaced at a distance $1/n$ of the previous spacing. This turns out to be a real convenience, so we set $d = d'/n$ and write the Bragg law in the form $\lambda = 2d \sin \theta$.

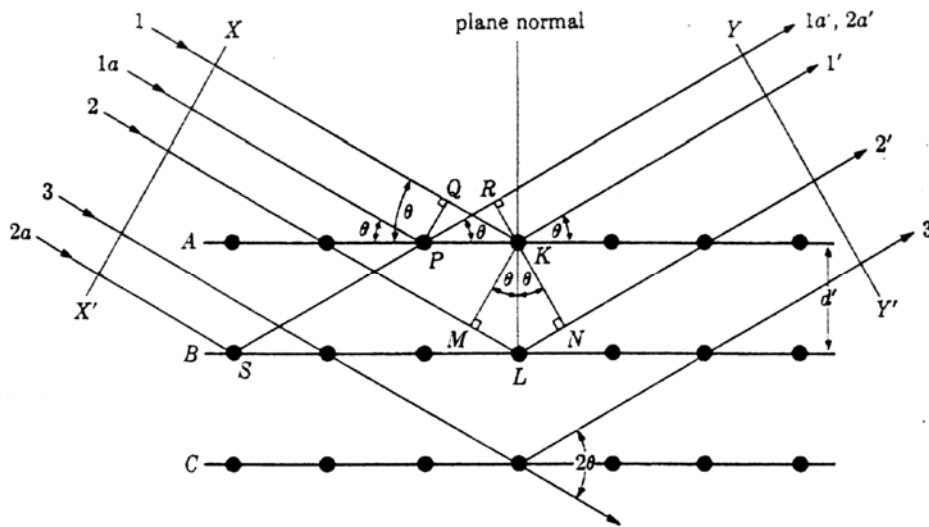


Fig. 2.1 Diffraction of X-ray

What determine the possible directions, referring to Fig. 2.2, we see that various diffraction angles $2\theta_1, 2\theta_2, 2\theta_3, \dots$ can be obtained from the (100) plane by using a beam incident at the correct angle $\theta_1, \theta_2, \theta_3, \dots$ and producing the first-, second-, third-, ...order reflections. But diffraction can also be produced by the (110) planes, the (111) planes, the (213) planes, and so on. We obviously need a general relation which predicts the diffraction angle for any set of planes. This relation is obtained by combing the Bragg law and the plane-spacing equation.

For example, The value of d , the distance between adjacent planes in the set (hkl) , if the crystal is cubic, then

$$\lambda = 2d \sin \theta \tag{2.4}$$

and

$$\frac{1}{d^2} = \frac{(h^2 + k^2 + l^2)}{a^2}, \quad (2.5)$$

where a is the lattice constant.

Combing these equations, we have

$$\sin^2 \theta = \frac{\lambda^2}{4a^2} (h^2 + k^2 + l^2). \quad (2.6)$$

This equation predicts, for a particular incident wavelength λ and a particular cubic of the unit cell size a , all the possible Bragg angle at which diffraction can occur from the planes (hkl) . For (110) plane, for example, Eq. (2-6) becomes $\sin^2 \theta_{110} = \frac{\lambda^2}{2a^2}$. If the crystal is tetragonal, with axes a and c , then the corresponding general equation is

$$\sin^2 \theta = \frac{\lambda^2}{4} \left(\frac{h^2 + k^2}{a^2} + \frac{l^2}{c^2} \right) \quad (2.7)$$

and similar equations can readily be obtained for the other crystal systems.

These examples show that the directions, in which a beam of given wavelength is diffracted by a given set of lattice planes, are determined by the crystal system to which the crystal belongs to and its lattice parameters. In short, diffraction directions are determined solely by the shape and size of the unit cell. This is an important point and so is its converse: all we can possibly learn about an unknown crystal by measurements of the directions of diffracted beams are the shape and size of the unit cell.

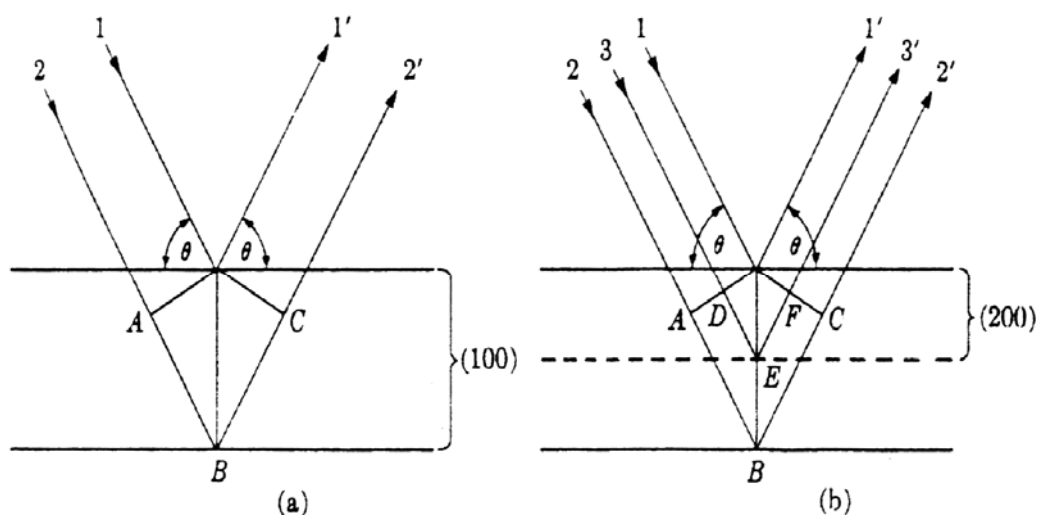


Fig 2-2 Equivalence of (a) a second-order 100 reflection and (b) a first-order 200 reflection.



2.2 Rietveld method

Rietveld analysis (1969) is a “whole pattern” treatment rather than a limited number of reflections of the X-ray data and it gives the type of structural analysis. Rietveld method requires the knowledge of approximate crystal structure of all phases of interest. The input data need to calculate a synthetic pattern include the space group symmetry, number of atoms, atomic positions, temperature factor, site occupancies, and lattice parameters. The refinement is conducted by minimizing the sum of the weighted, squared differences of this calculated pattern and the observed intensities every step in a digital powder patterns. In a refined procedure, individual scale factors (related to the weight percents of each phase) and profile, background, and lattice parameters, atomic positions, and site occupancies can be varied. [15-16]

2.2-1 Core Mathematics and Procedure

Many Bragg reflections contribute to the intensity y_i observed at many arbitrarily chosen points i in the pattern. The calculated intensities y_{ci} are determined from the $|F_k|^2$ calculated from the structural model by summing the calculated contributions from neighboring Bragg reflections plus background

$$y_{ci} = s \sum_k L_k |F_k|^2 \varphi(2\theta_i - 2\theta_k) P_k A + y_{bi} \quad (2.8)$$

where

s is the scale factor

k indicates for the Miller indices h , k , and l for a Bragg reflection

L_k contains the Lorentz polarization and multiplicity factors

F_k is the structure factor for the k -th Bragg reflection

φ is the reflection profile function

P_k is the preferred orientation function

A is an absorption factor

y_{bi} is the background intensity at the chosen position.

The best-fit sought is the best least-square fit to all of the data of y_i 's simultaneously.

The quantity minimized in the least-squares refinement is the residual S_y :

$$S_y = \sum_i w_i (y_i - y_{ci})^2 \quad (2.9)$$

where

$w_i = 1/y_i$ is weight factor

y_i is the observed intensity at the position i

y_{ci} is the calculated intensity at the position i .

2.2-2 Criteria of Fit

The Rietveld refinement process will adjust the refinable parameters until the residual Eq. (2.9) is minimized in some sense. A best fit will depend on the adequacy of the model and on whether a global minimum, rather than a local minimum is reached.

The Rietveld method have developed several common used R-values:

$$\text{R-pattern: } R_p = \frac{\sum |y_k(\text{obs}) - y_k(\text{cal})|}{\sum y_k(\text{obs})}, \quad (2.10)$$

$$\text{R-weighted pattern: } R_{wp} = \left\{ \frac{\sum w_i [(y_k(\text{obs}) - y_k(\text{cal}))^2]}{\sum w_i [y_k(\text{obs})]^2} \right\}^{1/2}, \quad (2.11)$$

$$\text{R-Bragg factor: } R_B = \frac{\sum |I_k(\text{obs}) - I_k(\text{cal})|}{\sum I_k(\text{obs})}, \quad (2.12)$$

where

I_k is the integral intensity assigned to the k-th Bragg reflection.

y_i is the intensity at the position i

$w_i = 1/y_i$ is weight factor

We can get the R_p and R_{wp} values form GSAS program. Here we choose R_{wp} values to discuss our refinement results.

When R_{wp} is less than 10%, the refinement is regarded as be reasonable.

2.2-3 The profile function

The profile function to fit is recommended using pseudo-Voigt profile function. The usual refinable functions are list below:

$$\text{Gaussian function: } \frac{C_0^{1/2}}{\pi^{1/2}H_k} \exp\left[\frac{-C_0(2\theta_i - 2\theta_k)^2}{H_k^2}\right], \quad (2.13)$$

$$\text{Lorentzian function: } \frac{C_1^{1/2}}{\pi H_k} \frac{1}{\left[1 + C_1 \frac{(2\theta_i - 2\theta_k)^2}{H_k^2}\right]}, \quad (2.14)$$

$$\text{Model 1 Lorentzian function: } \frac{2C_2^{1/2}}{\pi H_k} \frac{1}{\left[1 + C_2 \frac{(2\theta_i - 2\theta_k)^2}{H_k^2}\right]^2}, \quad (2.15)$$

$$\text{Model 2 Lorentzian function: } \frac{C_3^{1/2}}{2H_k} \frac{1}{\left[1 + C_3 \frac{(2\theta_i - 2\theta_k)^2}{H_k^2}\right]^{3/2}}, \quad (2.16)$$

$$\text{pseudo-Voigt fuction: } \eta L + (1 - \eta)G. \quad (2.17)$$

The parameter η can be defined as a linear function of 2θ in the NA and NB refinable variables, where NA and NB are refinable variables :

$$\eta = NA + NB \times (2\theta), \quad (2.18)$$

where H_k is the full width at half maximum (FWHM) of the k^{th} Bragg reflection and $C_0 = 4 \ln 2$, $C_1 = 4$, $C_2 = 4(2^{1/2} - 1)$, and $C_3 = 4(2^{3/2} - 1)$.

2.3 Raman scattering

When light passes through a medium, most of the light is reflected, transmitted, absorbed, elastic scattered, or inelastic scattered. Raman scattering is an inelastic scattering process. When the light encounters the medium, it interacts inelastically with phonon modes and produces outgoing photons whose frequencies are relatively shifted by an amount of energy corresponding to phonon energy from that of the incoming light. The scattered outgoing photons are called the Raman-scattered photons. If the light of frequency ν_0 is scattered by some media, the spectrum of the scattered light contains a strong line of frequency ν_0 and much weaker lines of frequencies $\nu_0 - \Delta\nu_1$, $\nu_0 - \Delta\nu_2$,, $\nu_0 + \Delta\nu_2$, $\nu_0 + \Delta\nu_1$, etc. Those lines on the low frequency side of the exciting lines (i.e. $\nu_0 - \Delta\nu_i, i = 1, 2, \dots$) are always matched by lines on the high frequency side (i.e. $\nu_0 + \Delta\nu_i, i = 1, 2, \dots$) but the latter are much weaker when the scattering medium is at room temperature. Raman scattering is inherently a weak process, but laser provides enough intensity that the spectra can be routinely measured. In analogy with terms used in the discussion of fluorescence spectra, lines on the low frequency side of the exciting line are known as Stokes lines and those on the high frequency side as anti-Stokes lines.

The incident photon loses its energy by producing a phonon (Stokes shifted), or gain energy and momentum by absorbing a phonon (anti-Stokes shifted), according to the energy and momentum conservation rules

$$h\nu_s = h\nu_i \pm h\Omega, \quad (2.19)$$

$$q_s = q_i \pm K, \quad (2.20)$$

where ν_i and ν_s are the incoming and the scattered photon frequencies, q_i and q_s are the incoming and the scattered photon wavevectors, Ω and K are the phonon frequency and wavevector, respectively.

All the Raman mode frequencies, intensities, line-shape, and line-width, as well as polarization behavior can be used to characterize the lattice and impurities. The

intensity gives information on crystallinity. The line-width increases when a material is damaged or disordered, because damage or disorder occurs in a material will increase phonon damping rate or relax the rules for momentum conservation in Raman process. All these capabilities can be used as a judgment for layered microstructure as well as bulk materials, subject only to the limitation that the penetration depth of the exciting radiation range from a few hundred nanometers to few micrometers.

2.4 Born effective charges and LO-TO splitting

The total polarization in the crystal can be expressed as a sum of contributions from the displacements of the charged ions and from the displacements of electrons relative to their ionic nuclei

$$P^i = P_{ion}^i + P_{electron}^i \quad (2.21)$$

and

$$P_{ion}^i = \frac{N}{V} \sum_{\alpha} e_{\alpha} U_{\alpha}^i, \quad (2.22)$$

where i is the label of Cartesian coordinate, N is the number of primitive cells in the crystal volume V and e_{α} is the charge of the α th ions in a primitive cell, all ions of the same label suffering the same displacement U_{α} .

It is convenient to express the ionic polarization in terms of the normal mode coordinates. The polarization is a vector, and the vibrational modes that contribute to the polarization are limited to those with the same symmetry character as a polar vector. These polar modes can be chosen so that their contributions to the polarization are parallel to the principal axes of the susceptibility tensor. Let ξ_{σ} be a unit vector parallel to the polarization contributed by the displacement of normal mode coordinates W_{σ} . Then one of the Cartesian components ξ_{σ}^i is unity and the other two are zero. The ionic polarization can be written as

$$P_{ion}^i = \frac{N}{V} \sum_{\sigma} Z_{\sigma} \xi_{\sigma}^i W_{\sigma}, \quad (2.23)$$

$$Z_{\sigma} \xi_{\sigma}^i \equiv \sum_{\alpha} \frac{e_{\alpha} c_{\alpha\sigma}^{i*}}{M_{\alpha}^{1/2}}, \quad (2.24)$$

where Z_{σ} is the effective charge of the normal mode σ and the mass of the α th atom is denoted by M_{α} . By the simplification equations of motion, we obtain

$$W_{\sigma} = \sum_{\alpha} W_{\alpha}^{1/2} c_{\alpha\sigma}^i U_{\alpha}^i, \quad (2.25)$$

where W_{α} is the displacement of the α th atom and the transformation coefficients $c_{\alpha\sigma}$ can be chosen to satisfy the orthonormality relations

$$\sum_{\alpha} c_{\alpha\sigma}^{i*} c_{\alpha\sigma'}^i = \delta_{\sigma\sigma'}. \quad (2.26)$$

The presence of an electric field E modifies the harmonic oscillator equation of the normal mode to

$$\ddot{W}_{\sigma} + \Gamma_{\sigma} \dot{W}_{\sigma} + \omega_{\sigma}^2 W_{\sigma} = Z_{\sigma} \xi_{\sigma}^i E^i. \quad (2.27)$$

The applied electric field of frequency ω , therefore, produces a steady-state normal-mode amplitude,

$$W_{\sigma} = \frac{Z_{\sigma} \xi_{\sigma}^i E^i}{\omega_{\sigma}^2 - \omega^2 - i\omega\Gamma_{\sigma}} \quad (2.28)$$

and the ionic polarization can be written in a form proportional to the electric-field components. We assume that ω is in the vicinity of the vibrational frequencies and well below the frequencies of all electric transitions. The relative permittivity is then

$$\kappa^i = \kappa_{\infty}^i + \sum_{\sigma} \frac{NZ_{\sigma}^2 \xi_{\sigma}^{i2} / \varepsilon_0 V}{\omega_{\sigma}^2 - \omega^2 - i\omega\Gamma_{\sigma}}, \quad (2.29)$$

where κ_{∞}^i is a constant electric contribution to the relative permittivity, so that

$$P_{electron}^i = \varepsilon_0 (\kappa_{\infty}^i - 1) E^i. \quad (2.30)$$

The electric field and polarization of any electromagnetic wave frequency ω and

wavevector q will satisfy the Maxwell's equations:

$$-\varepsilon_0 c^2 q(q \cdot E) + \varepsilon_0 (c^2 q^2 - \omega^2) E = \omega^2 P, \quad (2.31)$$

This equation is unfortunately very complicated in its most general form, but simplification can be made for most applications. The most striking simplification occurs when the frequency and wavevector satisfy $cq \gg \omega$. We obtained

$$\kappa_x q_x^2 + \kappa_y q_y^2 + \kappa_z q_z^2 = 0. \quad (2.32)$$

By combining the equation for the divergence of the electrical displacement

$$q \cdot (\varepsilon_0 E + P) = 0, \quad (2.33)$$

and Eqs. (2.32) and (2.33) two equations above, we can obtain the general representation

$$\ddot{W}_\sigma + \omega_\sigma W_\sigma = - \frac{NZ_\sigma(q \cdot \xi_\sigma) \sum_\tau Z_\tau(q \cdot \xi_\tau) W_\tau}{\varepsilon_0 V (\kappa_x q_x^2 + \kappa_y q_y^2 + \kappa_z q_z^2)}, \quad (2.34)$$

where τ is summed over all the polar modes. In cubic symmetry crystal, the polar-vector representation is threefold degenerate. The crystals are optically isotropic and the principal axes are not restricted to lie in any particular directions. For any direction of the wavevector of a threefold polar mode, it is permissible to choose two of the polarization vectors ξ_σ perpendicular to q and the third ξ_σ parallel to q . The two transverse polar modes have a frequency determined by the standard lattice dynamics calculation. The longitudinal polar mode has the associated macroscopic electric field, and its frequency is determined by the equation above, which reduces to

$$\kappa = 0 \quad (2.35)$$

in the cubic case. The simplest cases to consider first are the cubic crystals that have a single threefold polar mode. The relative permittivity has the isotropic form

$$\kappa = \kappa_\infty + \frac{NZ^2 / \varepsilon_0 V}{\omega_T^2 - \omega^2 - i\omega\Gamma}, \quad (2.36)$$

where the mode frequency ω_0 is replaced by ω_T to emphasize its transverse nature and redundant subscripts and superscripts are omitted. The longitudinal frequency obtained from the equation mentioned above with the damping removed is

$$\omega_L = \left(\frac{\kappa_0}{\kappa_\infty}\right)^{1/2} \omega_T, \quad (2.37)$$

where κ_0 is the zero-frequency value of the relative permittivity

$$\kappa_0 = \kappa_\infty + \frac{NZ^2}{\varepsilon_0 V \omega_T^2}. \quad (2.38)$$

This expression for the longitudinal frequency is the Lyddane-Sachs-Teller relation. The equation of motion for the longitudinal mode takes the form

$$\ddot{W} + \omega_T^2 W = -\frac{NZ^2 W}{\varepsilon_0 V \kappa_\infty}, \quad (2.39)$$

and leads to

$$\omega_L^2 = \omega_T^2 + \frac{NZ^2}{\varepsilon_0 V \kappa_\infty}. \quad (2.40)$$

Resta *et al.* [16] have shown that polarization is linear in the change of the position vector of the basis atom to a good approximation. The Born effective charge tensor Z_m^* is rewritten through

$$\delta P = \frac{e}{\Omega} \sum_{m=1}^N Z_m^* \cdot \delta u_m. \quad (2.41)$$

Here, N is the number of atoms in the primitive unit cell, δu_m is the first-order change of the position vector of the m th basis atom, and Ω is the volume of the unit cell.

The Born effective charge tensor reflects the effects of the Coulomb interactions and is directly related to the LO-TO splitting. The general representation of the dynamical material for LO and TO modes at $q=0$ are related by

$$D_{mn}^{LO} = D_{mn}^{TO} + \frac{4\pi e^2}{\Omega} \frac{Z_m^* Z_n^*}{\varepsilon_0}, \quad (2.42)$$

where D represents the dynamical matrix and is proportional to the square of the vibration frequency. Zhong *et al.*[11] and Waghmare *et al.* [17] have calculated that the softest TO mode is most associated with the hardest LO mode via Coulomb interaction to give rise to giant LO-TO splitting in ABO_3 compounds, especially for the ferroelectric phonon modes.

Chapter 3 Experimental details

3.1 Sample preparation

We modified the glycothermal treatment method[28] was adopted to synthesize BaTiO₃ nanocrystals to yield homogeneous samples with highly accurate composition. We will describe in detail the procedure of glycothermal method as follows.

Barium hydroxide octahydrate Ba(OH)₂·8H₂O was used as a source of Ba. Titanium tetrachloride TiCl₄ was used as a source of Ti. Throughout the process, the CO₂-free deionized water was used in the preparation of all aqueous solutions to prevent contamination of barium basic carbonates. Fig. 3-1 shows the procedure.

- (1) Modification of titanium tetrachloride was achieved by adding CO₂-free deionized water to prepare aqueous TiOCl₂ solution with Ti⁴⁺ concentration of 0.1M.
- (2) Amorphous titanium hydrous gel was prepared by adding 30 ml NH₄OH dropwise into 160ml 0.1M TiOCl₂ solution at 60°C for 2h with stirring.
- (3) The gel was separated and washed with CO₂-free water by three cycles of centrifugation for 4 min at 4000 rpm.
- (4) Excess water was decanted after final washing and the precursor was redispersed in a mixture of water and 1,4-butanediol.

- (5) $\text{Ba}(\text{OH})_2 \cdot 8\text{H}_2\text{O}$ was then added into a mixture of water and 1,4-butanediol, total solvent volume was 160ml.
- (6) Volume ratio of 1,4-butanediol/deionized water (B/W) from 8/0 to 0/8 with Ba/Ti molar ratio of 1 at temperature from 100°C to 220°C for 12h.
- (7) The resultant suspension was placed in stainless steel pressure vessel which was heated to the desired temperature with a rate of $3^\circ\text{C}/\text{min}$ for 12h.
- (8) The powders were washed with pH adjusted (pH ~ 10), CO_2 -free deionized water to remove the unreacted Ba in solution, and also prevent incongruent dissolution of the barium ions from the BaTiO_3 particle surface.
- (9) The powders were washed with acetic acid (0.1 mol) to remove and residual BaCO_3 and then washed with pH adjusted (pH ~ 10), CO_2 -free deionized water.
- (10) After washing, the recovered powders were dried at 60°C in a desiccator for 48h.

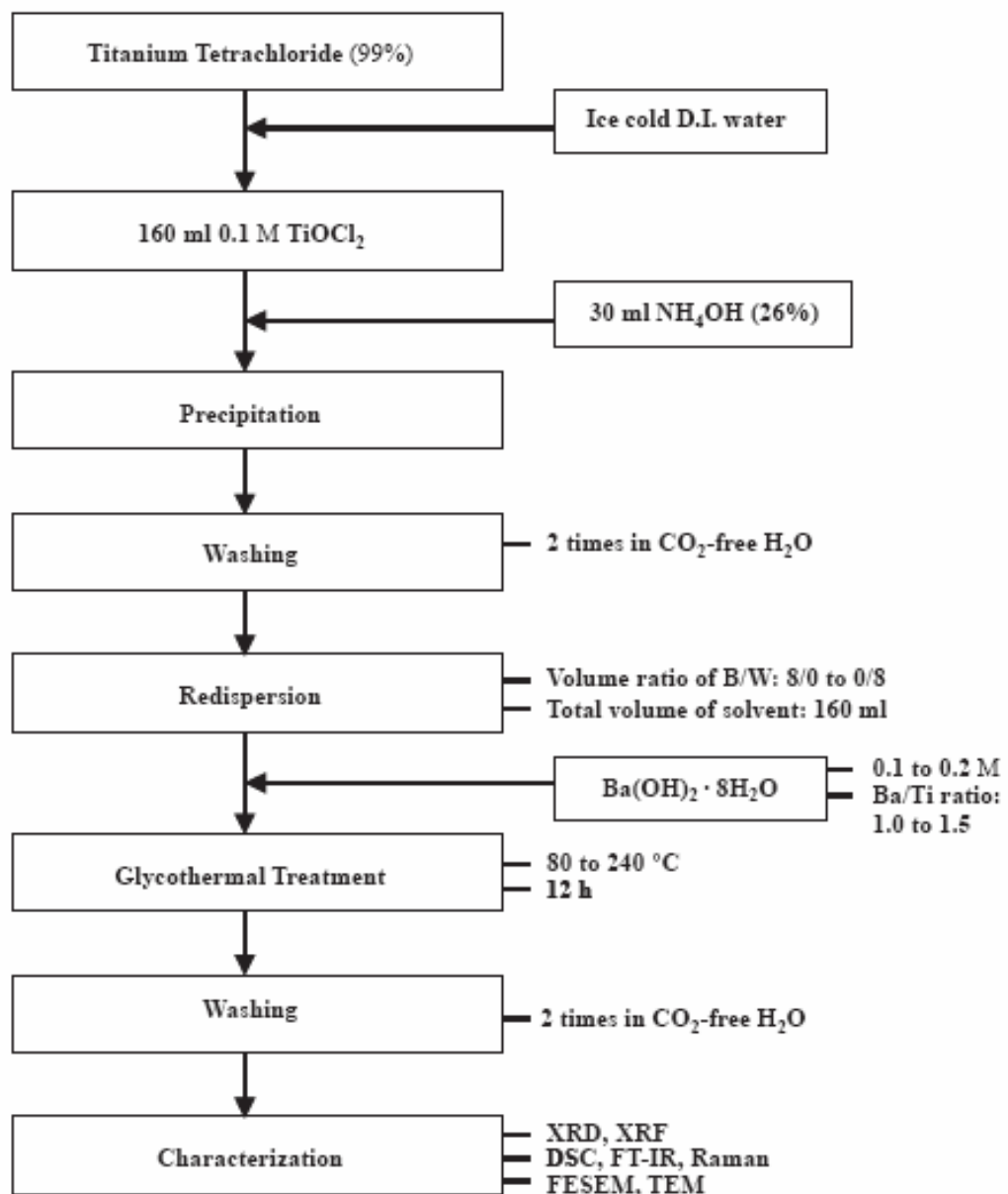


Fig. 3.1 Flowchart of BT solution obtained by glycothermal method

Ref. [28]

3.2 Characterization

3.2.1 X-ray diffraction system

The XRD data of the BaTiO₃ nanoparticles was collected on the imaging plate with transmission geometry using high intensity synchrotron radiation with wavelength of 0.56357Å at beam line BL01C synchrotron radiation facility, NSRRC, Taiwan.

3.2.2 Refinement system

The measured data were analyzed using Rietveld refinement. Rietveld refinement method is a method for Rietveld analysis of x-ray powder diffraction patterns. We use GSAS (General Structure Analysis System) program for the refinement of structure models to x-ray diffraction data. It is capable of handling all of these types of data simultaneously for given structural problems. GSAS has been created by Allen C. Larson and Robert B. Von Dreele of Los Alamos National Laboratory. (www.ncnr.nist.gov)

3.2.3 Raman detection system

Raman spectroscopy consists of mainly three components: laser system, spectrometer, and computer. Fig. 3.2 shows schematics of experimental setup. An Ar-ion laser (Coherent INNOVA 90) provides an excitation source at wavelength 488 nm. The spectra were measured at room temperature. The unwanted plasma lines were filtered out by a laser-line filter. A biconvex spherical lens with a focal length of 5 cm was used to focus the laser beam onto the sample surface at 45 degree

reflection geometry. The laser power on the sample surface is about 30~50 mW with beam spot size of 30~50 μm (in diameter). The scattered light was collected by a camera lens and imaged onto the entrance slit of a spectrograph (Spex triplamate1877C) which is equipped with a liquid-nitrogen cooled charge coupled device (CCD) detector array (Photometrics CCD 3000).

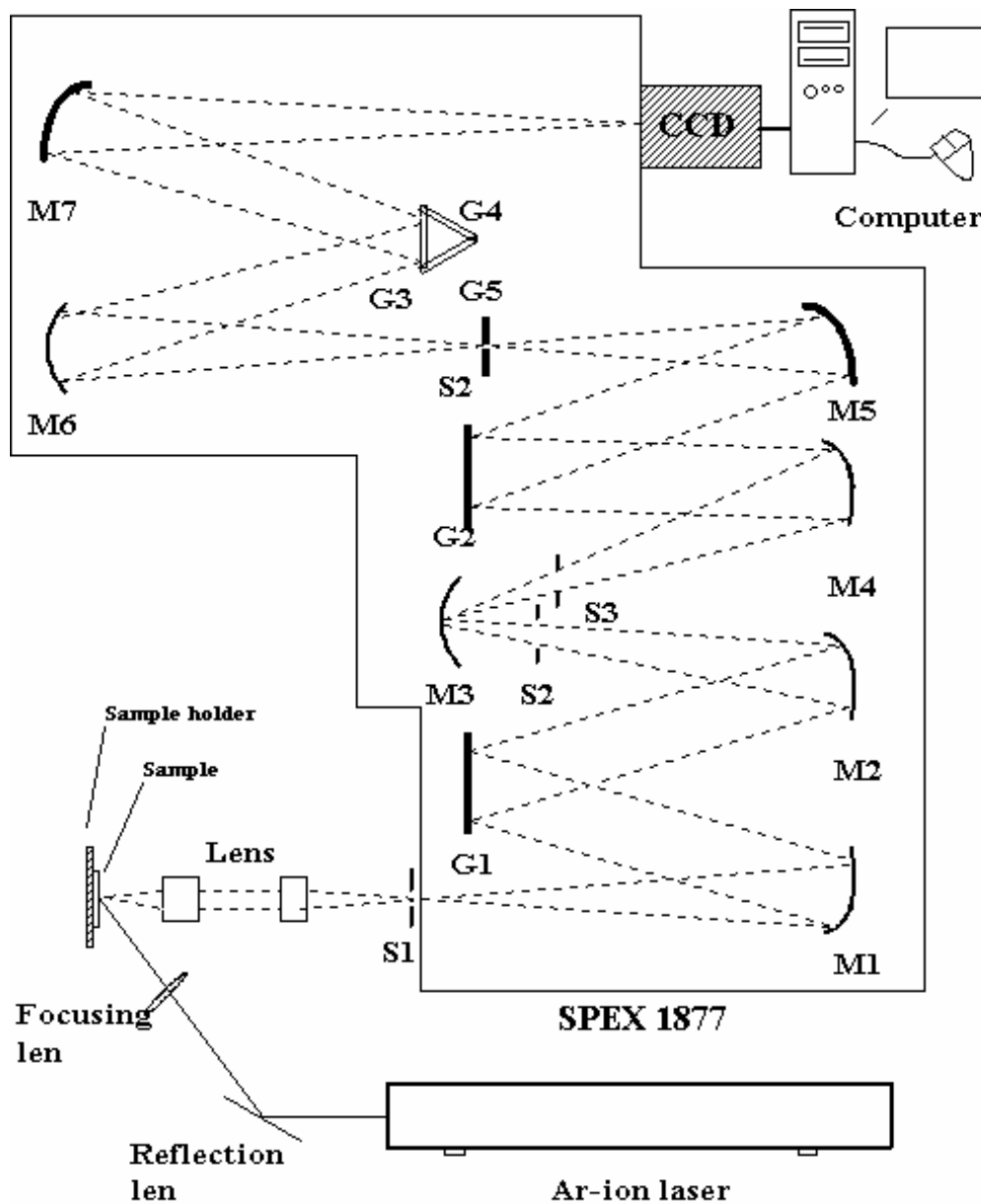
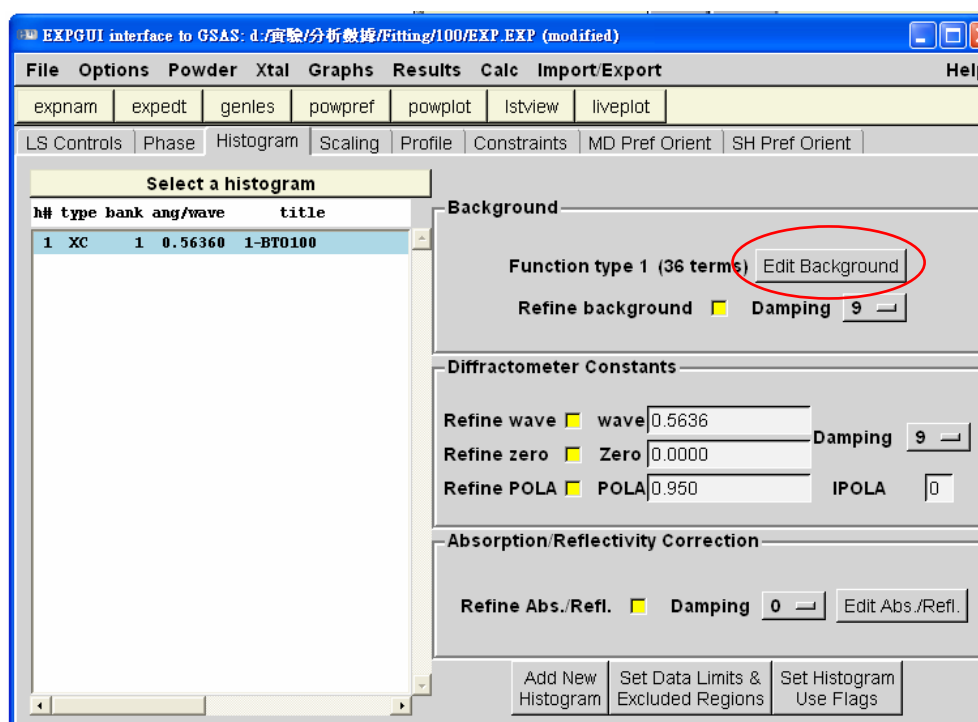


Fig. 3.2 Setup of Raman measurement

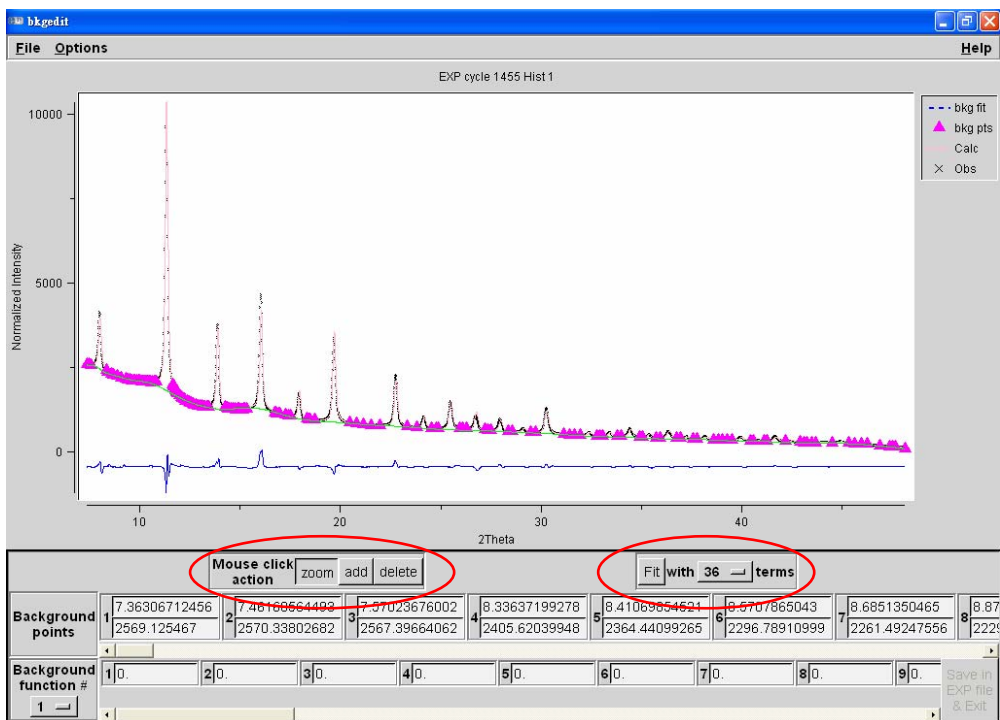
3.3 Refinement procedure

EXPGUI is a graphical interface for GSAS package. It can be used to directly modify the GSAS experiment file. We will describe in detail the procedure of refinement as follows.

- (1) Creating an experiment file.
- (2) Adding a phase: including space group, lattice constant, atoms positions.
- (3) Add data file to the Experiment: Specifying powder diffraction data (adding a Histogram) and instrument parameters.
- (4) Changing the Background Function: Pressing the button “Edit Background” to correct background. “Number of terms” can be set more terms to fit the background.

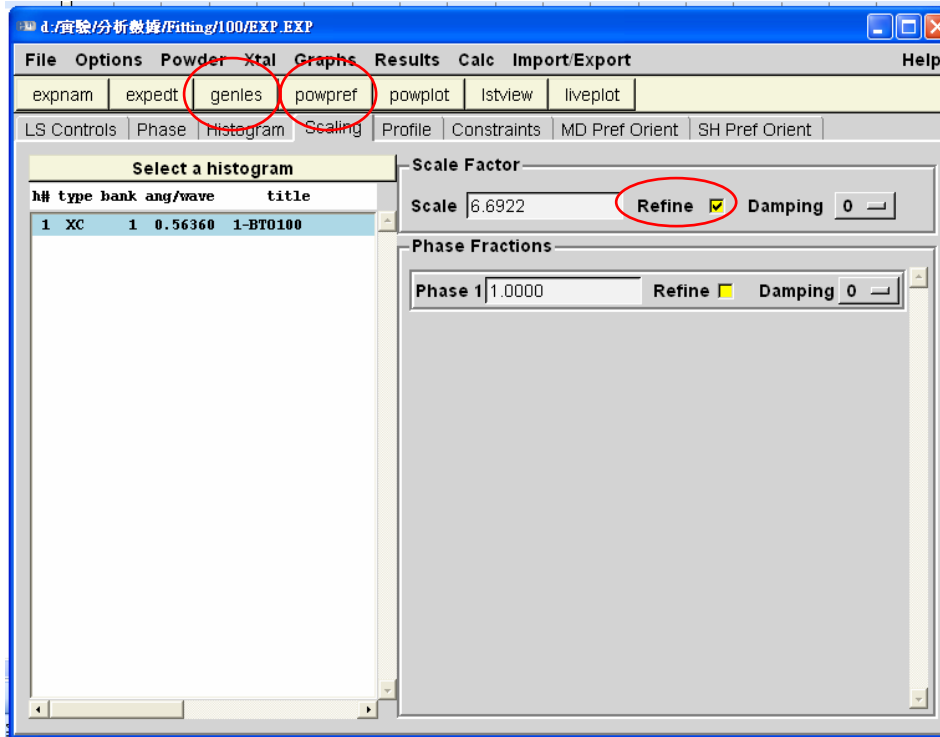


Note: The larger magnitude of damping means it converges and diverges faster.



(5) Initial Fitting: Refine “scale factor” (always open) and “background” (not refine at first). First run POWPREF by pressing the “POWPREF” button on the beige tool bar. Secondly, initiate the refinement, by launching the “GENLES” program to optimize the scale factor and background parameters.

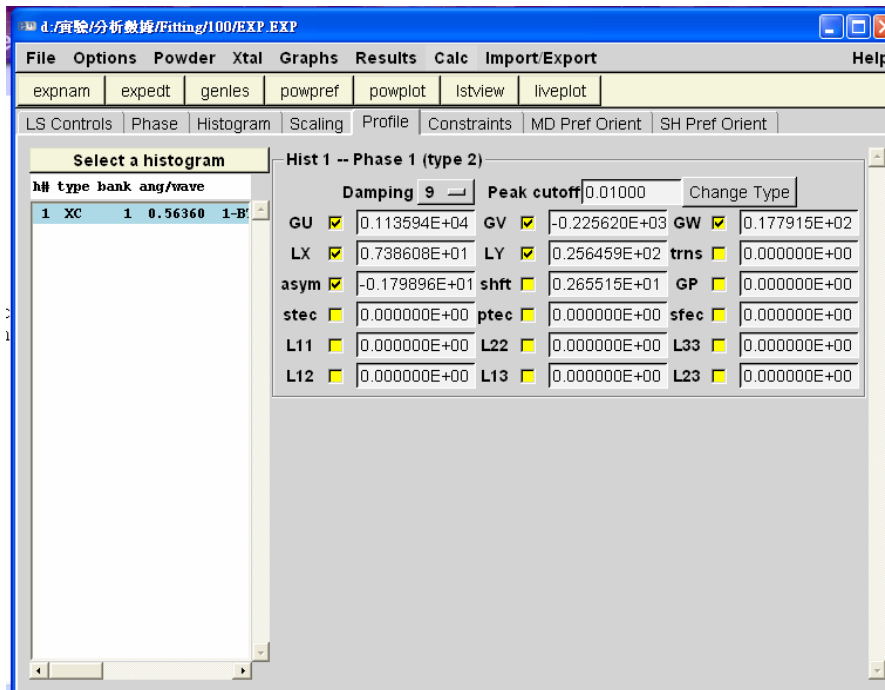
(6) Fitting the unit cell: zero can’t open with cell parameter



(7) Fitting of profile parameters :

Gaussian : GU 、GV 、GW (Gaussian profile function along x 、 y 、 z axes)

Lorentian : LX (particle size) 、LY (microstrain)



(8) Refine coordinates and overall U_{iso} (thermal parameters): The reasonable values of U_{iso} between $0.025/4 \sim 0.025 \times 4$

(9) Refine background

Note: The reasonable values of scale < 99 . If it diverges, we can reset to 1.

If initial fitting graph is too narrow, we can set GW larger to refit.

When fitting background, other parameters must close.

Changing sequences of fitting parameters depends on fitting graph.



Chapter 4 Results and Discussion

4.1 Results of the SEM patterns

BaTiO₃ nanoparticles shown in FESEM micrographs of Fig. 4.1 have low aggregation and narrow size distribution with mean diameters of about 140, 60, and 30 nm, respectively.

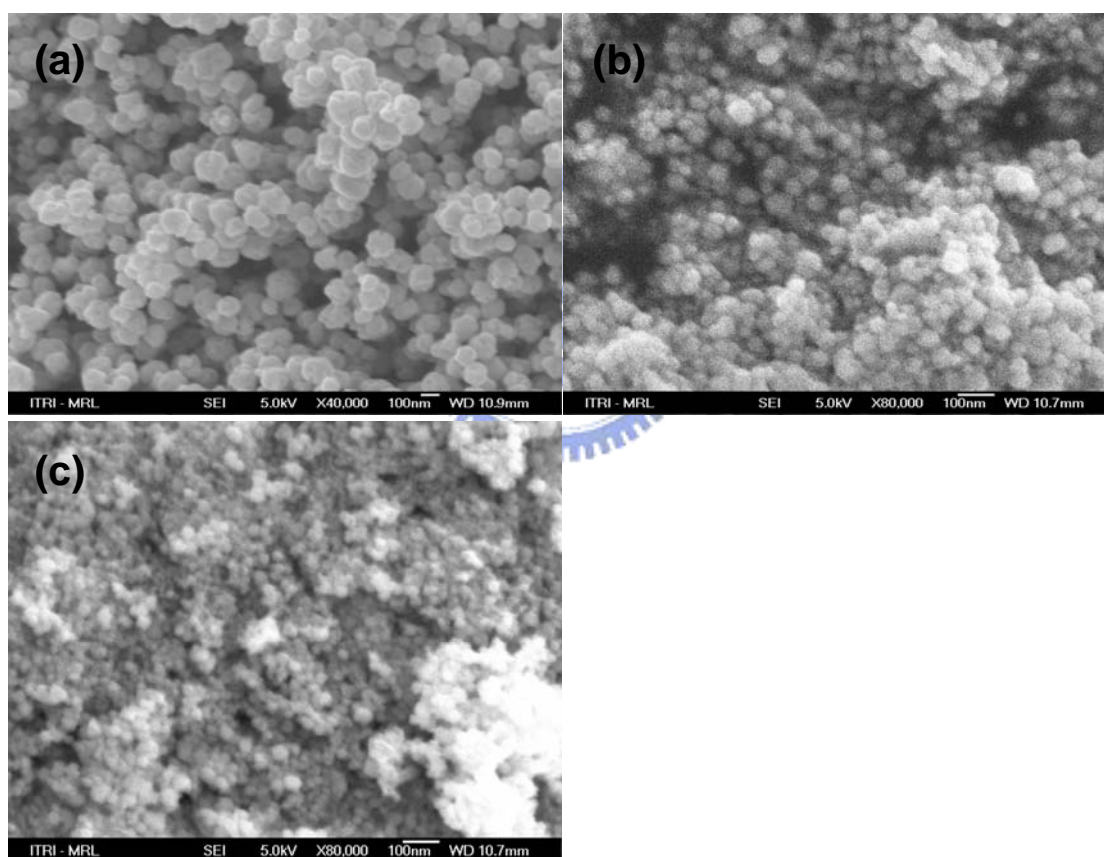


Fig. 4.1 SEM patterns of BaTiO₃ samples with various mean diameters (a) 140nm (b) 60nm (c) 30nm

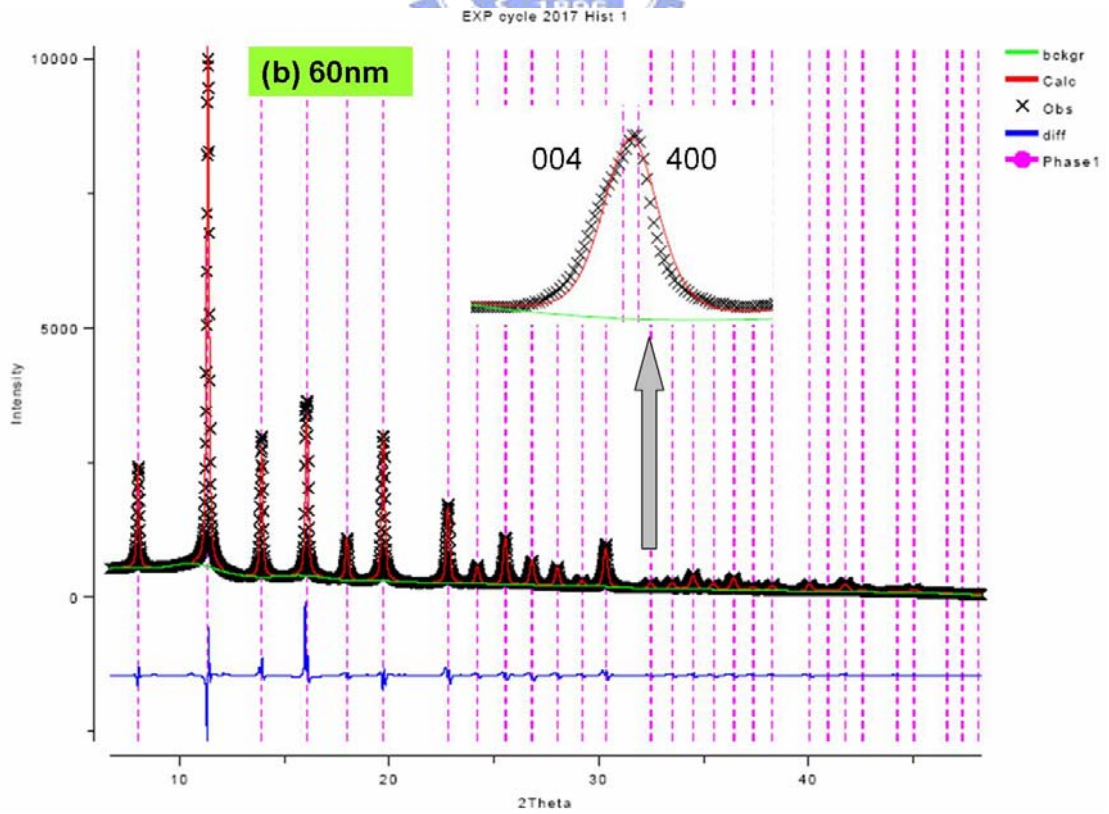
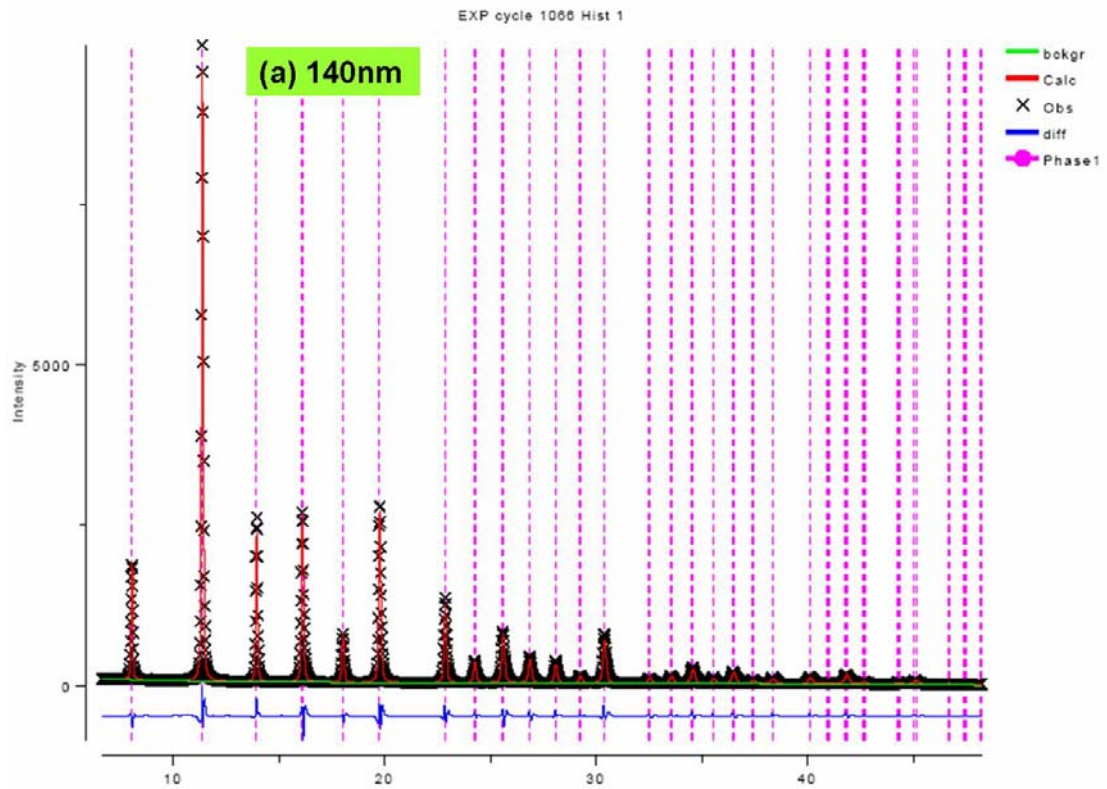
4.2 Analysis of Rietveld refinement

To analyze the crystal symmetry of BaTiO₃ nanoparticles, high resolution diffraction patterns of various sizes of BaTiO₃ nanoparticles were taken by using high-energy synchrotron radiation x-ray and refined by using the GSAS program. We choose profile function as Rietveld function, setting constraint, then refining the parameters by sequence and sequence. Table 4.1 shows the initial refinement conditions.

Crystal system : tetragonal				
Space group : P4mm				
Lattice parameter : a = b = 3.994, c = 4.038, $\alpha = \beta = \gamma = 90^\circ$				
Atomic type	x	y	z	U _{iso}
Ba	0	0	0	0.025
Ti	0.5	0.5	0.512	0.025
O1	0.5	0.5	-0.026	0.025
O2	0	0.5	0.5	0.025

Table 4.1 The structural parameter of BaTiO₃

Figure 4.2 shows results and differences after Rietveld refinement for nanoparticles with sizes of 140 nm, 60 nm, and 30 nm. The observed and calculated profiles agree well. The profile around 40° in 2θ for 60 nm-sized BaTiO₃ particles exhibited a shoulder splitting into (224) and (422) due to the difference in the lengths between the a and c axes of the tetragonal phase. Hence we can use a tetragonal single phase (P4mm) model to refine the crystal structure with the XRD data. Note that we also did the same analysis for particle size larger 1 μm (labeled as bulk) for comparison.



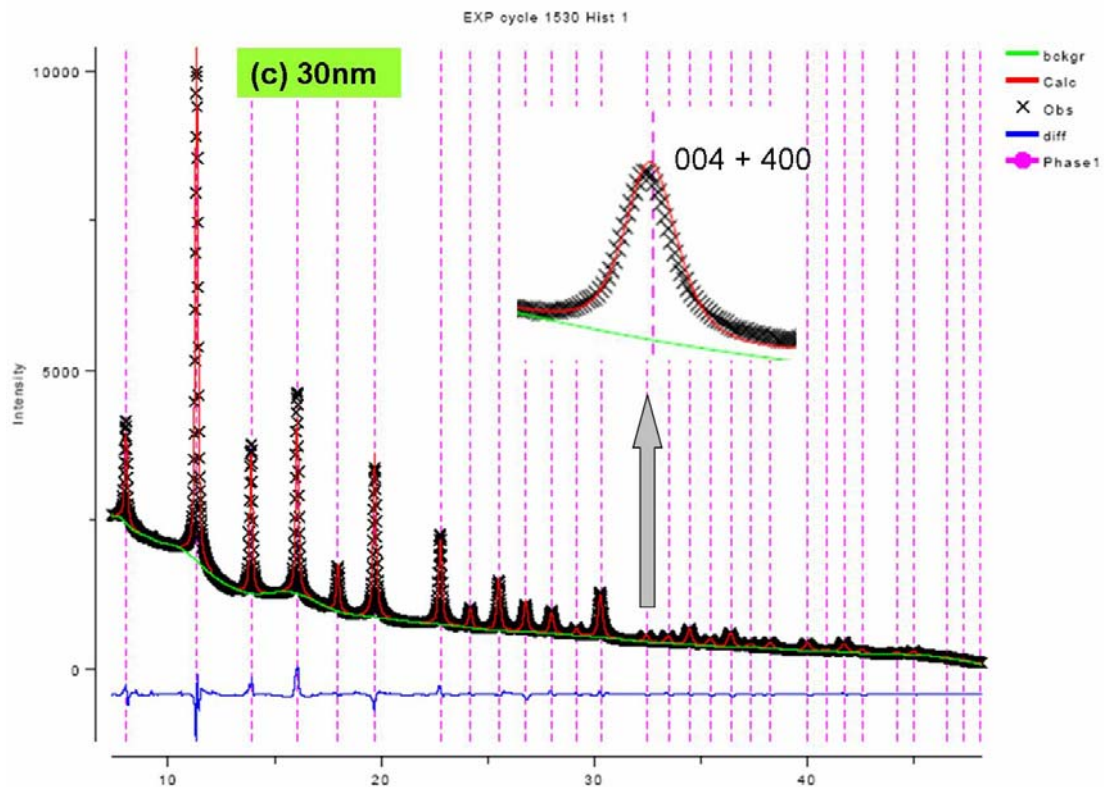


Fig. 4.2 Rietveld patterns for various BaTiO_3 particle size. Particle size are (a) 140nm (b) 60nm (c) 30nm. An enlarged profile around the (004) and (400) reflection peaks is inserted to show the splitting.

The refined structure parameters and reliability factors for nanoparticles with sizes of 140, 60, and 30 nm were listed in Table 4.2. Refined positional parameters of the tetragonal BaTiO_3 suggested small displacements of oxygen atoms and Ti atom along the c axis. The lattice constants a and c, shown in Fig 4.3, simultaneously relax with decreasing the particles size. The results are consistent with the assumption proposed by Ishikawa, *et al.* [17] Fig. 4.4 shows that the tetragonality

(c/a) declines from 1.0026 to 1.0008 with expanding unit-cell volume, in both of a and c axes, as the particle size decreases from 140 nm to 30 nm. The unit-cell volume of the tetragonal BaTiO₃ increases with decreasing particle size, as shown in Fig. 4.4.

Particle size	~ μm (ref.)	140 nm	60 nm	30 nm
R_{wp}		11.20%	7.46%	2.78%
a (\AA)	3.9940	4.01995	4.02845	4.03289
c (\AA)	4.006	4.03043	4.03573	4.03615
c/a	1.003	1.00261	1.00181	1.00081
Atomic coordinate (Ti)		(0.5,0.5,0.53395)	(0.5,0.5, 0.52012)	(0.5,0.5, 0.51842)
Atomic coordinate (O1)		(0.5,0.5, 0.02987)	(0.5, 0.5, 0.01595)	(0.5,0.5, 0.00611)
Atomic coordinate (O2)		(0, 0.5, 0.50923)	(0, 0.5, 0.50959)	(0, 0.5, 0.50737)

Table 4.2 Refined structure parameters and reliability factors for BaTiO₃ nanoparticles at RT.

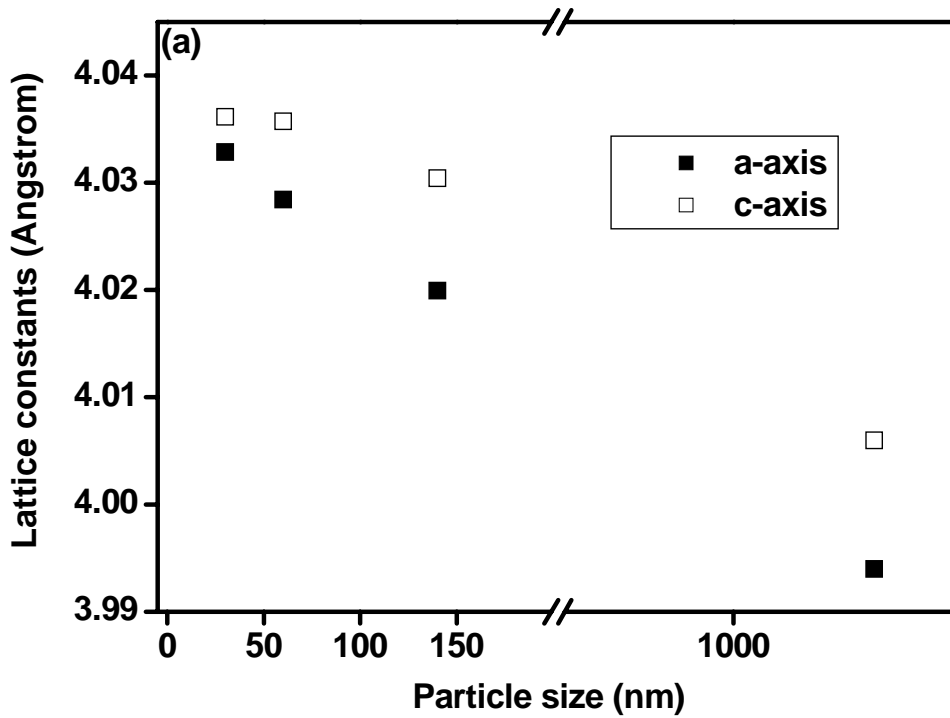


Fig. 4.3 Lattice constant a and c of BaTiO₃ nanoparticles after Rietvelt refinement procedure

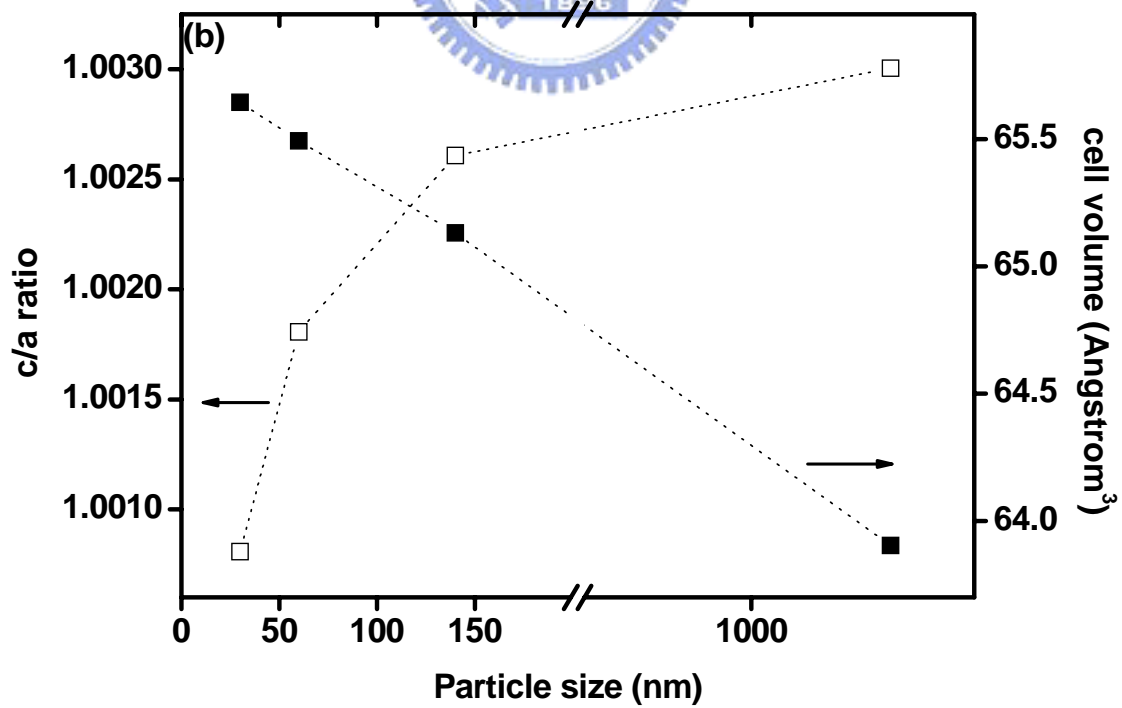


Fig. 4.4 Lattice constant ration c/a and cell volume of BaTiO₃ nanoparticles after Rietvelt refinement procedure

The trend of phase transition for our synthesized BaTiO₃ nanoparticles with decreasing particle size agrees with other previous reports. [3,8-12] Nevertheless, our results of XRD refinement reveal the critical size of BaTiO₃ nanoparticles, which is the size of the phase transition from tetragonal to cubic at RT, may be smaller than 30 nm, that differs from the argument reported by Yashima, *et al.*, [12] in which the size-induced phase transition occurs between 40 nm and 30 nm. According to Table I, the refined atom positions in a unit cell of the tetragonal BaTiO₃ nanoparticles suggest less displacement of titanium and oxygen (O1) atoms along the c axis with decreasing particle size.

4.3 Analysis of the Raman spectra

The Raman spectra of BaTiO₃ nanoparticles taken at RT were plotted in Fig. 4.5 with particle sizes of 30 nm, 60 nm, 140 nm, and > 1 μm (bulk from Ref. 7), respectively.

Around 180 cm⁻¹ which is assigned to A₁(TO₁) phonon mode has a spectral dip for the bulk sample but that for nanoparticles becomes a spectral peak. A broad band around 260 cm⁻¹ attributed to A₁(TO₂) mode, a band at 305 cm⁻¹ to B₁ and E(TO+LO) modes, the asymmetric band around 520 cm⁻¹ to E(TO) and A₁(TO₃) modes, and the highest frequency band around 720 cm⁻¹ to A₁(LO) and E(LO) phonon modes, respectively. The observed Raman spectral peak positions of BaTiO₃ nanoparticles agree well with those reported by Yashima, *et al.* [11,12] However, even with size of 30 nm we did not observe Raman modes resulting from the hexagonal phase as observed in Ref. [12] That phenomenon is consistent with our results of GSAS refinement.

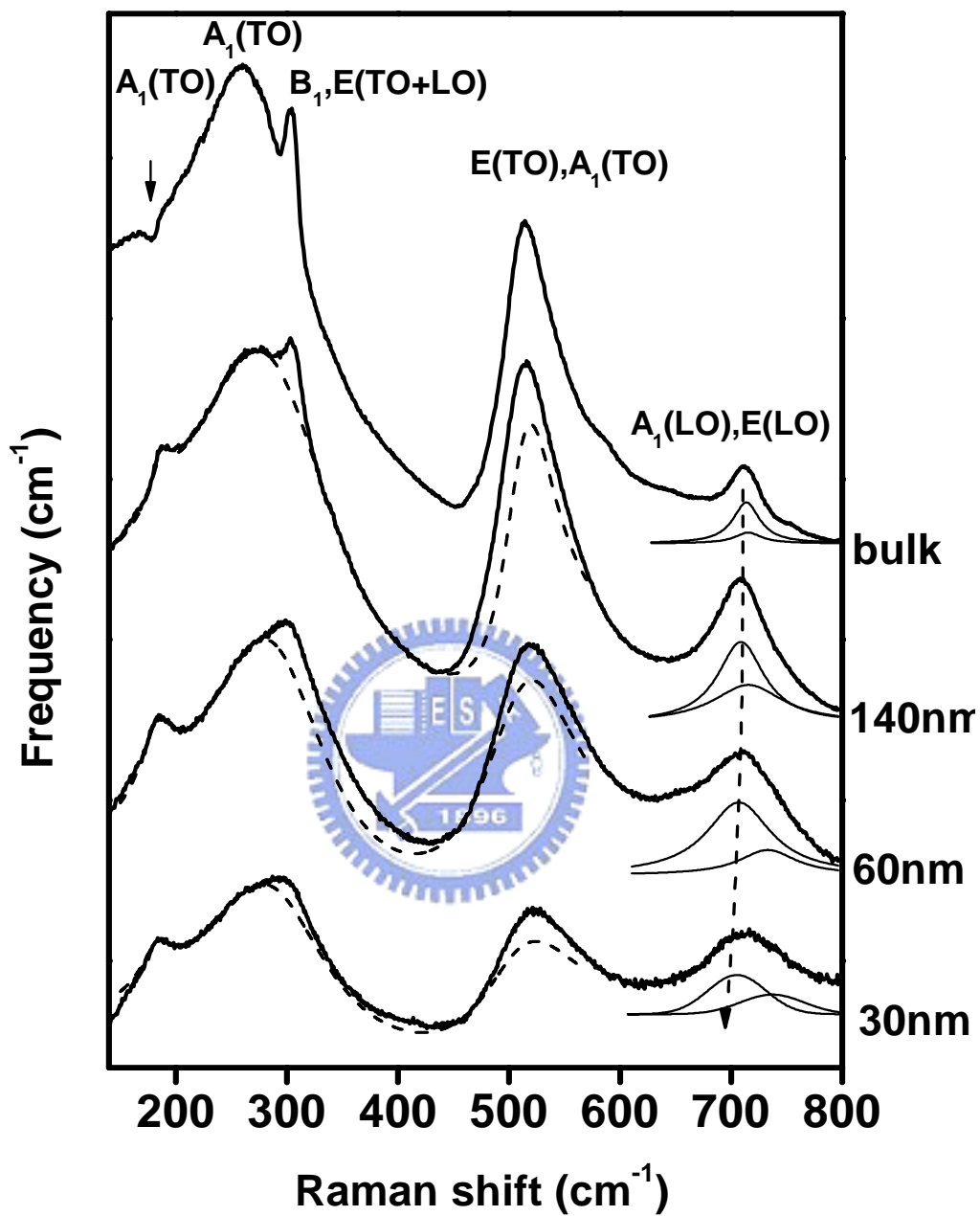


Fig. 4.5 Size dependence of Raman spectra for various size BaTiO₃. Bulk (> 1 μm) and nanoparticles of diameter 140, 60, and 30nm, respectively.

As the size decreases from bulk to nanoparticles, we found spectral peaks at 180 cm^{-1} in all the nanoparticles are basically located at the same frequency of the destructive interference dip for the bulk BaTiO_3 . The results indicate that the anharmonic phonon coupling maybe dependent on the grain size. The phonon modes at 305 and 720 cm^{-1} specific to the tetragonal phase of BaTiO_3 as described in Ref. [18] become weak and broad with decreasing particle size. In comparison with the results of XRD, the observed broadening of Raman peaks indicates that the crystal structure becomes progressively less tetragonal factor due to less displacements of Ti and O1 atoms.

As forementioned, the three $A_1(\text{TO})$ modes are strongly coupled together and two of them are heavily damped in the tetragonal phase of ABO_3 . In order to ascertain the influence of the coupling phenomenon, Sood [19] and Chaves *et al.* [20] have considered three individual phonon coupled $A_1(\text{TO})$ modes to distinguish them from the Raman spectra. The Raman intensity of the three coupled modes can be expressed as

$$I(\omega) = A [n(\omega) + 1] \text{Im}[\mathbf{T}^* \mathbf{G} \mathbf{T}], \quad (1)$$

where the inverse matrix response is

$$\mathbf{G}^{-1}(\omega) = \mathbf{\Omega}^2 - \omega^2 \mathbf{I} - i\omega \mathbf{\Gamma}, \quad (2)$$

A is a constant, $[n(\omega) + 1]$ is Bose-Einstein factor, \mathbf{T} is a vector involving Raman scattering amplitudes, \mathbf{I} is the unit matrix, $\mathbf{\Omega}^2$ is the force constant matrix, and $\mathbf{\Gamma}$ the damping matrix:

$$\mathbf{\Omega}^2 = \begin{pmatrix} \omega_1^2 & \omega_{12}^2 & 0 \\ \omega_{12}^2 & \omega_2^2 & \omega_{23}^2 \\ 0 & \omega_{23}^2 & \omega_3^2 \end{pmatrix}, \quad \mathbf{\Gamma} = \begin{pmatrix} \Gamma_1^2 & 0 & 0 \\ 0 & \Gamma_2^2 & 0 \\ 0 & 0 & \Gamma_3^2 \end{pmatrix}. \quad (3)$$

Here ω_i and ω_{ij} ($i, j=1,2,3$) are the frequencies of uncoupled modes and the coupling strength between modes i and j . The coupling between the lowest (ω_1) and the highest (ω_3) modes was set to zero ($\omega_{13} = 0$) to allow less fitting parameters. This is a reasonable approximation because they are too far from each other. Hence they have no spectral superimposition.

The asymmetric broad band around 500-600 cm^{-1} is attributed to superposition of $E(\text{TO})$ and $A_1(\text{TO}_3)$ modes. We find the results of polarized Raman study on the epitaxial BaTiO_3 film by Marssi, *et al.*, [21] the $E(\text{TO})$ mode is situated at the low frequency shoulder with about 1/4 intensity of the $A_1(\text{TO}_3)$ mode. Hence, it is reasonable to extract the contribution of the $E(\text{TO})$ mode about 1/4 compare to the intensity of $A_1(\text{TO}_3)$ mode for these randomly oriented nanoparticles. Besides, the fitting results will not show the difference from that if the contribution of $E(\text{TO})$ is ignored. The fitted parameters are plotted in Fig. 4.6 that allows us to clarify the coupling behavior of phonon with decreasing particle size.

We found that the coupling strength, ω_{12} , between ω_1 and ω_2 dramatically changes from 85 cm^{-1} to nearly zero as the particle size decreases from few micrometers to nanometers. The weaker (or zero) coupling between ω_1 and ω_2 in BaTiO_3 nanoparticles leads to observe a spectral peak around 180 cm^{-1} $A_1(\text{TO}_1)$ phonon mode for the nanoparticles rather than a dip for bulk at the same position. Figure 4.7 shows the as-read peak positions of three A_1 -symmetric TO modes from our Raman data (labeled as $A_1(\text{TO}_i)$, $i = 1,2,3$). These data obtained from the uncoupled-phonon model sign as hollow symbols and that obtained from the coupled-phonon model sign as solid symbols. From Fig. 4.7 we can see that the size-dependent decoupled (calculated) phonon frequency ω_1 overlaps with the

as-read $A_1(\text{TO}_1)$ so it again reveal weak coupling strength ($\omega_{12} \sim 0$). Due to decreasing the particle size with less tetragonality or small c/a , we found that the approach of uncoupled ω_2 and ω_3 results in slightly increasing in ω_{23} . The stronger coupling strength ($\omega_{23} \sim 300 \text{ cm}^{-1}$) makes these two modes approach. Therefore the measured $A_1(\text{TO}_2)$ peak slightly shifts toward the higher frequency and the measured $A_1(\text{TO}_3)$ peak slightly shifts toward the lower frequency upon decreasing the particle size.

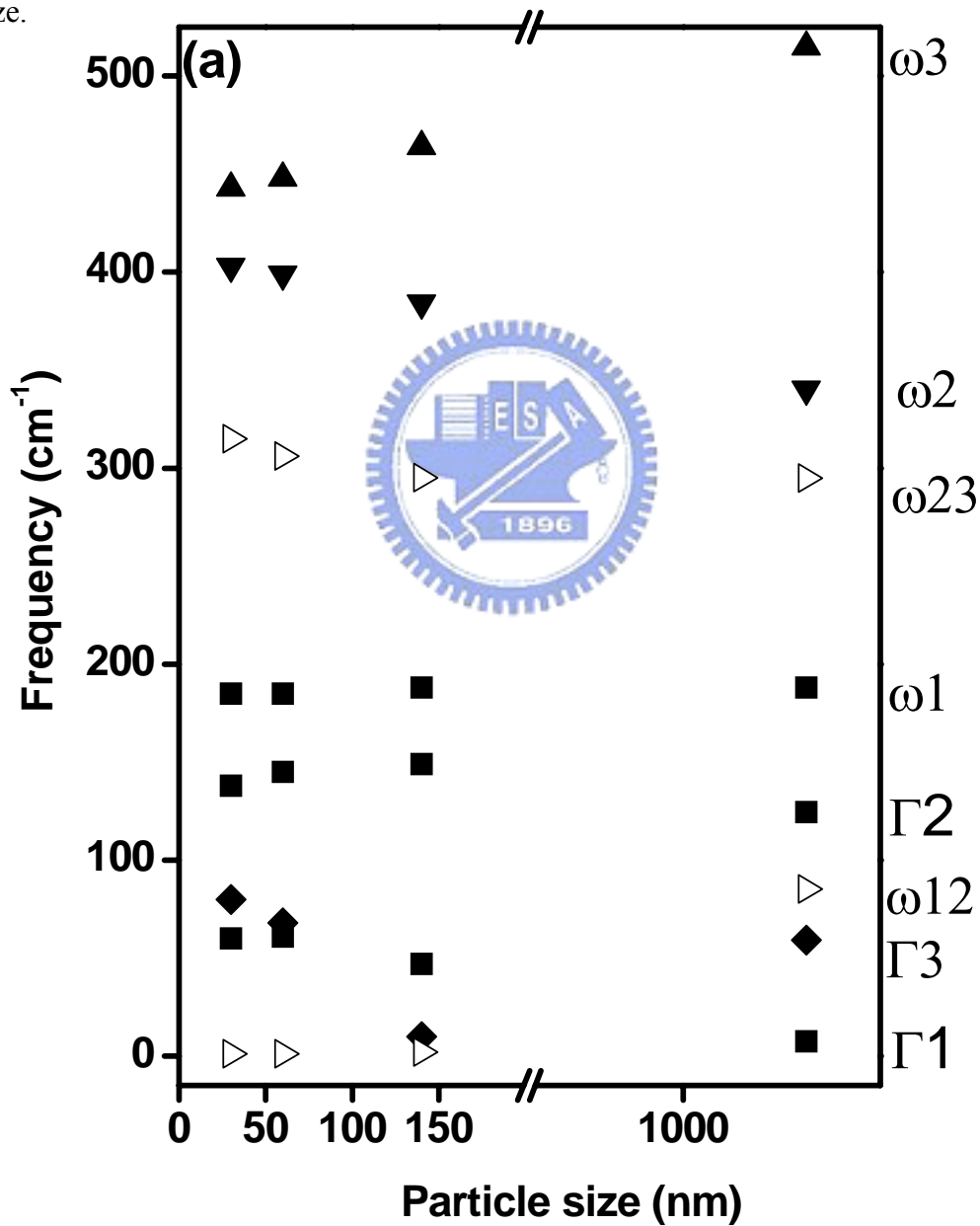


Fig. 4.6 The fitted parameters using the coupled-phonon mode plotted as a function of particle size.

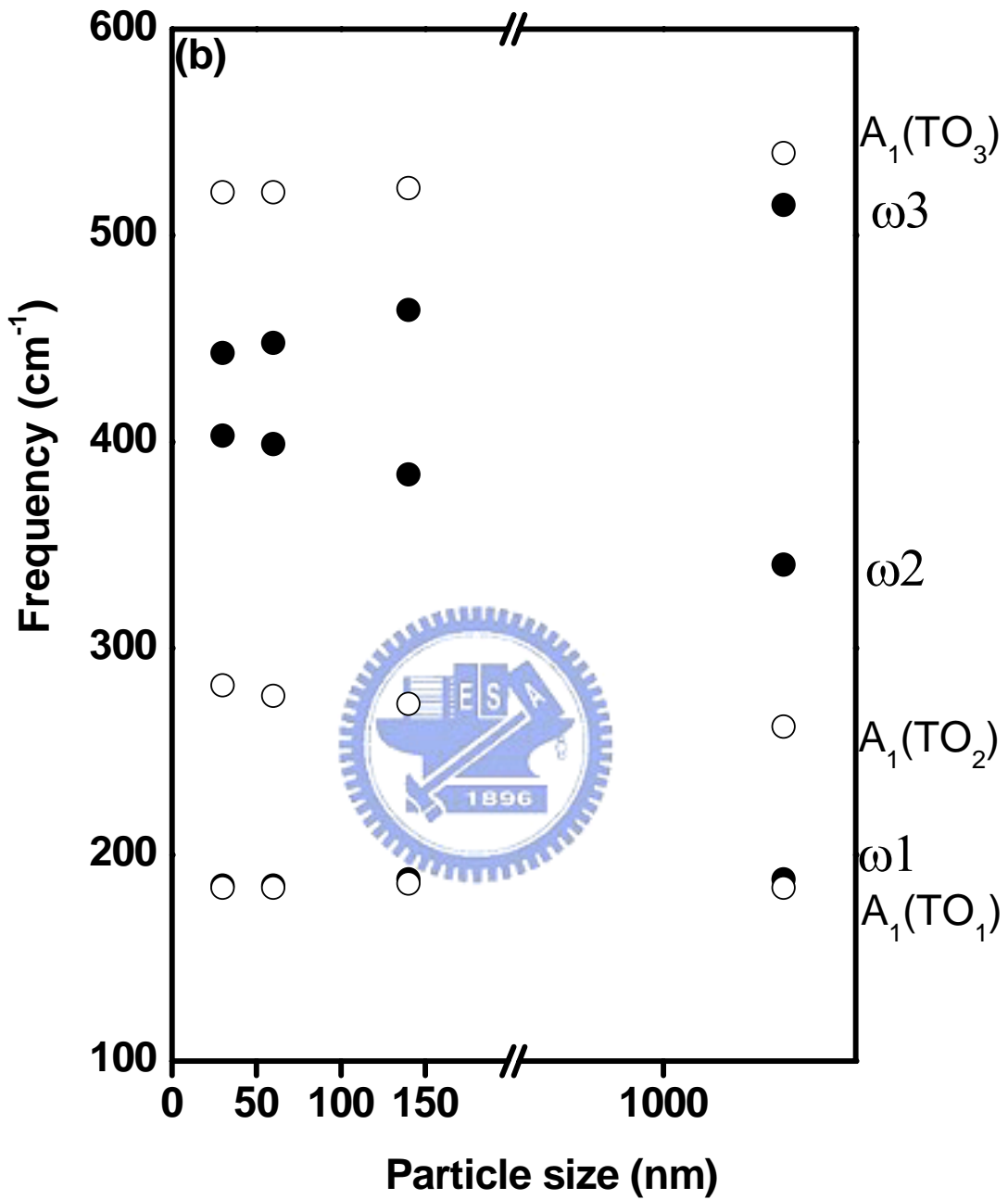


Fig. 4.7 The as-read peak positions from the data and the decoupled frequencies plotted as a function of particle size.

According to the calculation of Born effective charges of ABO₃ perovskites by Zhong *et al.*, [14] we comprehend that the calculated mode effective charge for the softest TO mode is the largest as listed in Table III of Ref. 14. It means that the softest TO mode will couple most strongly with the electric field. Due to strong mode mixing via Coulomb interaction, the softest TO mode [A₁(TO₁)] is the most closely associated with the hardest LO mode A₁(LO₃) that gives rise to giant LO–TO splitting in ABO₃ structure, especially for the ferroelectric phonon modes. The general representation of the dynamical matrices for LO and TO modes at $q = 0$ are related by

$$D_{mn}^{LO} = D_{mn}^{TO} + \frac{4\pi e^2}{V} \frac{Z_m^* Z_n^*}{\epsilon_\infty(0)}, \quad (4)$$

where D represents the dynamical matrix that is proportional to the square of the vibration frequency, V is the volume of the unit cell, $\epsilon_\infty(0)$ is the optical dielectric constant at $q = 0$, and Z^* is the Born effective charge of the corresponding vibration. The Coulomb interaction would play an important role in the behavior of LO-TO splitting.

According to the polarized Raman results [21], the asymmetric broad band near 750 cm⁻¹ in Fig. 4.5 can be resolved as A₁(LO) mode and a lower intensity E(LO) mode at the higher frequency side. From the decomposed result reported in Ref. (21), the intensity of E(LO) mode locates at the higher frequency is about 1/3 intensity of the A₁(LO) mode for BaTiO₃ bulk. With decreasing the particle size, the spectra still keep the same trend of the higher intensity for the A₁(LO) mode than for the E(LO) mode.

Fig. 4.8(a) shows the square difference of A₁(LO) and A₁(TO₁) modes phonon frequencies versus BaTiO₃ particle size. We observe the decreasing trend of LO-TO

splitting as the particle size decreases from $> 1\mu\text{m}$ to 30 nm, and that phenomenon agree with the inference of Ref. [14]. Since Ba-based ABO_3 perovskites basically possesses ionic bonding [22-25], the Born effective charge would not be influenced by changing the structure. From our results of Fig. 4.4, the unit cell dimension increases when the particle size decreasing from micrometer size to 30 nm. According to the general representation of the dynamical matrices for LO and TO modes at $q = 0$, we can expect reducing LO-TO splitting when unit cell dimension increase.

Fig. 4.8(b) shows the normalized square difference of $A_1(\text{LO})$ and $A_1(\text{TO}_1)$ modes phonon frequencies and normalized unit cell volume versus BaTiO_3 particle size. We observe the $4\pi e^2 \frac{Z_m^* Z_n^*}{\epsilon_\infty(0)}$ can be regarded as a constant, because the difference between the normalized square difference of $A_1(\text{LO})$ and $A_1(\text{TO}_1)$ modes phonon frequencies and normalized unit cell volume is very small. We can expect unit cell dimension is the dominated factor for LO-TO splitting.

Previously, we reported that the tetragonality declines with unit-cell volume decreasing as x changes from 1 to 0.7 in polycrystalline $\text{Ba}_x\text{Sr}_{1-x}\text{TiO}_3$. [7] Neglecting the change of effective charge due to the substitution, the variation of the unit-cell volume was considered be the dominant mechanism of increasing the LO–TO splitting in $\text{Ba}_x\text{Sr}_{1-x}\text{TiO}_3$ system. In compare to that study, we directly observe the decreasing LO-TO splitting when declining the tetragonality as decreasing the size of BaTiO_3 nanoparticles. That causes expansion of the unit-cell volume. We conclude that the change of unit-cell volume is also the dominant mechanism for the tendency of the LO–TO splitting in BaTiO_3 system without complicated ion replacement.

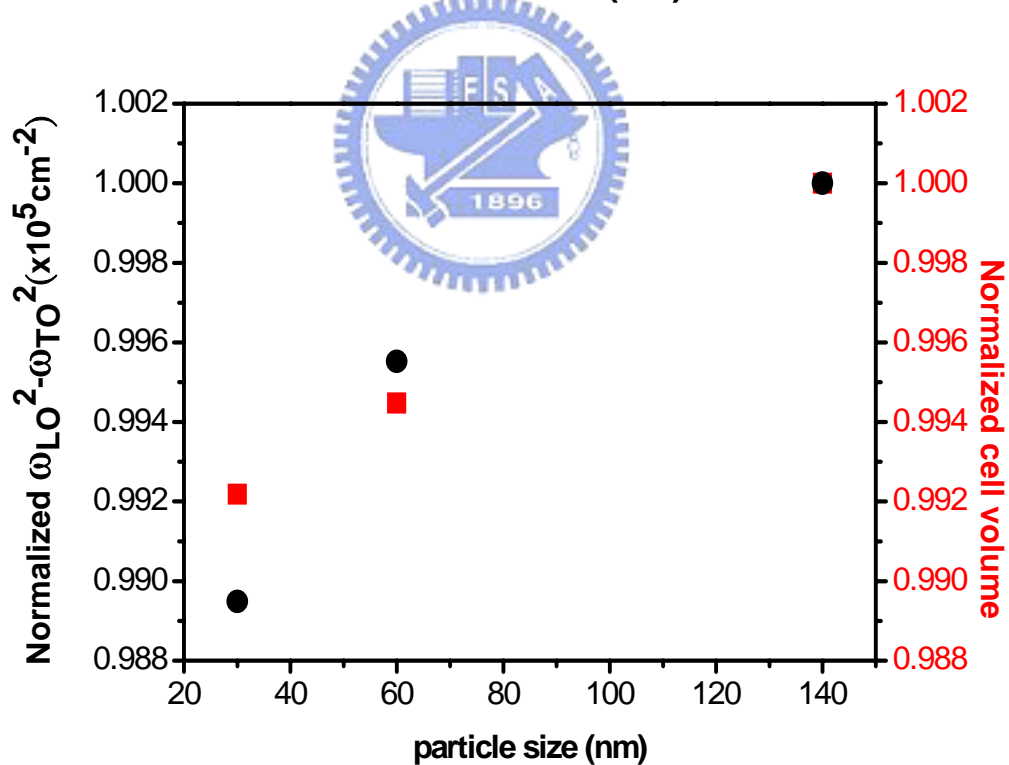
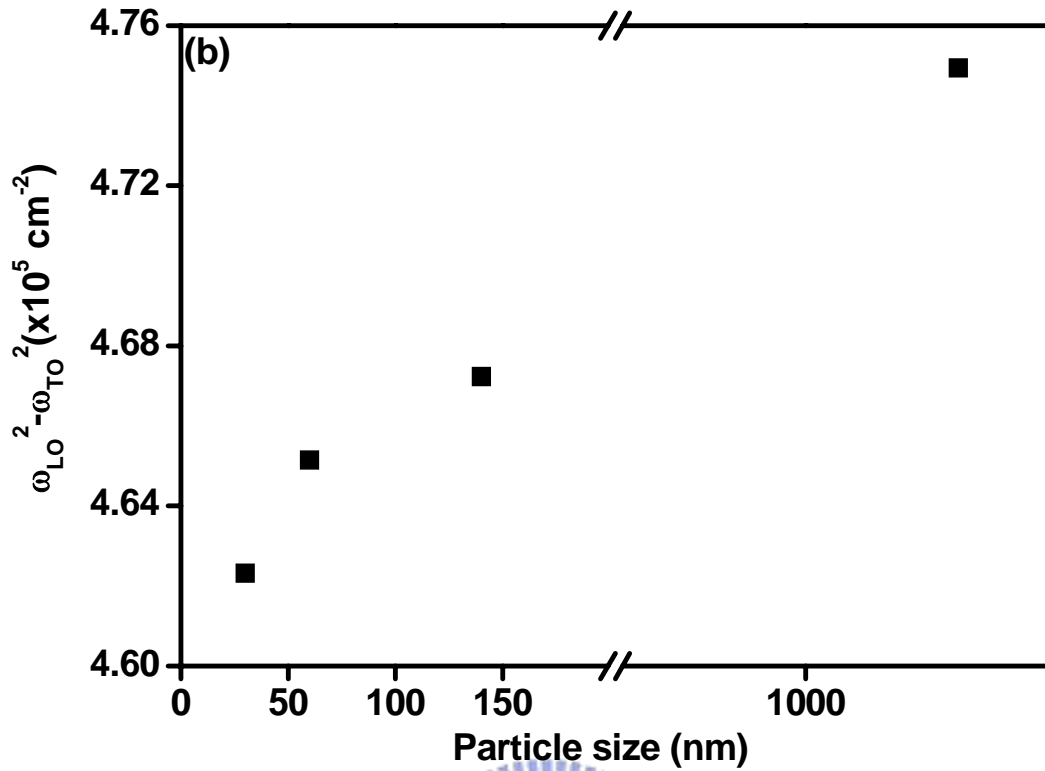


Fig. 4.8 Size dependent LO-TO splitting. (a) The difference between square of A1(LO₃) and A1(TO₁) phonon frequencies. (b) Normalized difference between square of A1(LO₃) and A1(TO₁) phonon frequencies and normalized cell volume.

Chapter 5 Conclusion


5.1 Conclusion

In summary, we have investigated the size effect on crystal structure of BaTiO₃ nanoparticles synthesized by the glycothermal method by using FESEM, high-resolution synchrotron XRD, and Raman spectroscopy. The crystal structure was made use of a single tetragonal-phase model to refine XRD data by Rietveld analysis of GSAS program. A enlarging unit-cell volume was confirmed with decreasing particle size. The large cell volume could be ascribed to (1) some lattice defects, (2) the surface effect of the fine particles, and (3) the metastable state in the chemical reaction from the intermediate amorphous phase to the tetragonal BaTiO₃ with a large c/a ratio.

We explained that the experimental evidence of weaker strength coupling between $A_1(\text{TO}_1)$ and $A_1(\text{TO}_2)$ leads to a change from a spectral dip at 180 cm^{-1} for $A_1(\text{TO}_1)$ phonon to a peak at the same position. We also found that the approach of uncoupled ω_2 and ω_3 with less tetragonality due to decreasing the particle size results in slightly increasing in ω_{23} . According to the results of decomposition, the spectra still keep the same trend of the higher intensity for the $A_1(\text{LO})$ mode than the $E(\text{LO})$. We also observed the decreasing LO-TO splitting with the decline of tetragonality when expansion of the unit-cell volume. Therefore, the change of unit-cell volume is the dominant mechanism for the tendency of the LO-TO splitting in BaTiO₃ system without complicated ion replacement.

5.2 Future work

Enormous interest in nanostructured materials for photonic applications has emerged in recent years. One class of such materials is represented by rare-earth doped nanocrystals that have been investigated for use as phosphors in amplifiers, lasers, and imaging for biological systems. The promising optical properties of rare-earth doped nanocrystals for photonic applications such as Led are investigated of frequency upconversion. Presently it is recognized that the upconversion efficiency depends on the nanoparticle shape, the site symmetry, and the statistical distribution of active ions. Also, the process of miniaturizing materials to the nanometer scale revealed that the radiative electronic relaxation probabilities of rare-earth ions doped in dielectric nanoparticles may be significantly different from their bulk counterparts.



We will synthesize Er-doped BaTiO₃ nanoparticles to investigate the luminescence properties of size dependent effects. In particular our interest is concerned with the structural changes occurring in nanoparticles Er-doped BaTiO₃ with different sizes and the investigation of their luminescence properties by evaluation of Ω parameters form the Judd-Ofelt theory.[26-27]

References

1. L. E. Cross, Am. Ceram. Soc. Bull., 63, 586-90 (1984).
2. D. H. Yoon and B. I. Lee, J. Eur. Ceram. Soc. 24, 753 (2004)
3. R. Pirc and R. Blinc, Phys. Rev. B 70, 134107 (2004)
4. J. Iñiguez and D. Vanderbilt, Phys. Rev. Lett. 89, 115503 (2002)
5. D. Damjanovic, F. Brem, and N. Setter, Appl. Phys. Lett. 80, 652 (2002)
6. U. D. Venkateswaran, V. M. Naik, and R. Naik, Phys. Rev. B 58, 14256 (1998)
7. S. Y. Kuo, W. Y. Liao, and W. F. Hsieh, 64, 224103 (2001)
8. M. H. Frey and D. A. Payne, Phys. Rev. B 54, 3158 (1996)
9. S. Tsunekawa, S. Ito, T. Mori, K. Ishikawa, Z.Q. Li, and Y. Kawazoe, Phys. Rev B 62, 3065 (2000)
10. Z. Zhao, V. Buscaglia, M. Viviani, M. T. Buscaglia, L. Mitoseriu, A. Testino, M. Nygren, M. Johnsson, and P. Nanni, Phys. Rev. B 70, 024107 (2004)
11. T. Hoshina, H. Kakemoto, T. Tsurumi, S. Wada, and M. Yashima, J. Appl. Phys. 99, 054311 (2006)
12. M. Yashima, T. Hoshina, D. Ishimura, S. Kobayashi, W. Nakamura, T. Tsurumi and S. Wada J. Appl. Phys. 98, 014313 (2005)
13. C. N. R. Rao and K. J. Rao: Phase Transitions in Solids (McGraw-Hill International Book Company, 1978).
14. W. Zhong, R. D. King-Smith and D. Vanderbilt, Phys. Rev. Lett. 72, 3618 (1994).

15. The Rietveld Method, R.A. Young, Oxford university press (1993)
16. Manual of GSAS software, A.C. Larson and R.V. Dreele, Los Alamos National laboratory (2000)
17. K. Ishikawa and T. Uemori, Phys. Rev. B 60, 11841 (1999)
18. R. Naik, J. J. Nazarko, C. S. Flattery, U. D. Venkateswaran, V. M. Naik, M. S. Mohammed, G. W. Auner, J. V. Mantese, N. W. Schubring, A. L. Micheli, and A. B. Catalan, Phys. Rev. B 61, 11367 (2000).
19. A. K. Sood, N. Chandrabhas, D. V. S. Muthu, and A. Jayaraman, Phys. Rev. B 51, 8892 (1995).
20. A. Chaves, R. S. Katiyar, and S. P. S. Porto, Phys. Rev. B 10, 3522 (1974)
21. M. El Marssi, F. Le Marrec, I. A. Lukyanchuk, and M. G. Karkut, J. Appl. Phys. 94, 3307 (2003).
22. R. E. Cohen, Nature (London) 358, 136 (1992)
23. Y. Kuroiwa, S. Aoyagi, and A. Sawada, Phys. Rev. Lett. 87, 217601 (2001).
24. Shou-Yi Kuo, Chung-Ting Li, and Wen-Feng Hsieh, Appl. Phys. Letts. 81(16) , 3019 (2002).
25. J. C. Jan, H. M. Tsai, C. W. Pao, J. W. Chiou, K. Asokan, K. P. Krishna Kumar, W. F. Pong, Y. H. Tang, M.-H. Tsai, S. Y. Kuo, and W. F. Hsieh, Appl. Phys. Letts. 87, 012103 (2005).
26. B. R. Judd, Phys. Rev. 127, 750 (1962)
27. G. S. Ofelt, J. Chem. Phys. 37, 511 (1962)
28. Yong-Jin Jung, Dae-Young Lim, Jun-Seok Nho, Seung-Beom Cho, Richard E. Riman, Byeong Woo Lee J. Cryst. Growth. 274, 638 (2005).